https://doi.org/10.5194/egusphere-2024-1477
Preprint. Discussion started: 12 June 2024

Development of high-order global dynamical core using discontinuous Galerkin method for atmospheric LES and proposal of test cases: SCALE-DG v0.8.0

Yuta Kawai[1] and Hirofumi Tomita[1,2]

[1]RIKEN Center for Computational Science, Kobe, Japan
[2]RIKEN Cluster for Pioneering Research, Wako, Japan

Correspondence: Yuta Kawai (yuta.kawai@riken.jp)

Abstract. Focusing on future global atmospheric simulations with grid spacing of O(10–100 m), we developed a global nonhydrostatic atmospheric dynamical core with high-order accuracy by applying discontinuous Galerkin method (DGM) both horizontally and vertically. Further, considering a global large-eddy simulation (LES), a Smagorinsky–Lilly turbulence model was introduced to the proposed global dynamical core in the DGM framework. By conducting several tests with various polynomial orders (p), the impact of high-order DGM on atmospheric flows was investigated. To show high-order numerical convergence, a few modifications were made in the experimental setup of existing test cases. In addition, we proposed an idealized test case to validate global LES models, which is a global extension of idealized planetary boundary layer (PBL) turbulence experiment performed in our previous studies. The error norms from the deterministic test cases, such as linear advection and gravity wave test cases, show an optimal order of spatial accuracy with about $p+1$-order when the temporal and round-off errors are sufficiently small. In the climatic test cases, such as the Held-Suarez test, the kinetic energy spectra indicate the advantage of effective resolutions when large polynomial orders are used. In the LES experiment, the global model provided a reasonable vertical structure of PBL and energy spectra since the results under shallow atmosphere approximation well reproduce those obtained in the plane computational domain.

1 Introduction

Recently developed supercomputers have enabled us to conduct high-resolution global atmospheric simulations using a subkilometer horizontal grid spacing (e.g., Miyamoto et al., 2013). In near future, this continuous development of computer technology is expected to perform global simulations using O(10–100 m) grid spacing (Satoh et al., 2019), which begin to explicitly represent turbulence in the inertia sub-range. Then, large-eddy simulation (LES) is a promising strategy. In LES, the turbulence with spatial scale larger than a spatial filter is explicitly calculated, whereas the effect of turbulence with smaller spatial scale is parameterized by eddy viscosity and diffusion terms.

Considering future high-resolution atmospheric simulations such as global LES, we discussed the problem of low numerical accuracy of conventional atmospheric dynamical cores in Kawai and Tomita (2021, 2023) (hereafter referred to as KT2021 and KT2023, respectively). To perform LES precisely, we should take care that the discretization errors do not dominate over

https://doi.org/10.5194/egusphere-2024-1477
Preprint. Discussion started: 12 June 2024

sub-grid scale (SGS) terms of turbulent models. Otherwise, the physical meaning of SGS terms is likely to be lost. KT2021 investigated the order of accuracy necessary for advection schemes in the framework of conventional grid-point methods. The study indicated that the advection scheme requires at least seventh- or eighth-order accuracy to ensure that the values of e-folding time with numerical diffusion and dispersion errors are sufficiently larger than those with diffusion and dispersion terms from the SGS terms. However, in the conventional grid-point methods, the required stencil becomes large with increasing order of accuracy. This can degrade computational performance of the schemes in recent massive parallel computers. Thus, we recently focused on the discontinuous Galerkin method (DGM), which is recognized as a local spectral method. At element boundaries, the representation of flow field is allowed to be discontinuous, and common flux shared by two neighbor elements is calculated using Riemann solvers. Such computational features provide a straightforward strategy to achieve high-order discretization and computational compactness. In the context of DGM, KT2023 investigated the problem with the order of accuracy necessary for LES. It indicated that the polynomial order needs to be higher than or equal to four in the case where upwind numerical flux and sufficiently high-order modal filter are used.

In the state-of-the-art global nonhydrostatic atmosphere dynamical cores whose basis was mainly developed during 2000–2010, low-order grid-point methods are often adopted; For example, the Non-hydrostatic ICosahedral Atmospheric Model (NICAM; Tomita and Satoh, 2004; Satoh et al., 2014), the Model for Prediction Across Scales (MPAS; Skamarock et al., 2012), and the ICOsahedral Non-hydrostatic model (ICON; Zängl et al., 2015) are based on either a totally first- or second-order scheme. The discretization accuracy has not always been a primary factor in the performance of atmospheric models because physical processes have various uncertain parameters. In situations where the grid spacing is coarser than the gray zone of turbulence, the totally second-order scheme may be appropriate in terms of both computational cost and numerical robustness. However, as described above, it is important to increase numerical accuracy to precisely conduct the atmospheric LES. Furthermore, even in spatial resolutions lower than that required by LES, it is undesirable that the effective resolution is significantly apart from the grid spacing in terms of the physics-dynamics coupling. The low-order dynamical cores typically lead to significant discretization errors at wavelengths shorter than eight grid spacing. To decrease the gap between the effective resolution and grid scale, it is natural to use high-order discretization methods in addition to designing better numerical filters for controlling the effective resolution.

Constructing high-order grid-point methods tends to be more complex for spherical geometries than that in plane domains with structured grids. To archive the high-order discretization accuracy horizontally, a spectral transformation method based on the spherical harmonics expansion is a straightforward traditional approach. It provides sufficient accuracy for numerical solutions in the wavelength range up to truncated wave number while avoiding the pole problem. However, in significantly high-resolution global simulations, we can suffer from large costs of data communication between all computational nodes in massive parallel supercomputer environments. On the other hand, some researchers have successfully developed global non-hydrostatic atmospheric dynamical cores based on high-order grid-point and element-based methods. Ullrich and Jablonowski (2012b) proposed a high-order finite volume method (FVM) with a fourth-order reconstruction strategy for horizontal discretization. The Tempest model (Ullrich, 2014; Guerra and Ullrich, 2016) uses a high-order spectral element method horizontally. The Climate Machine used a nodal discontinuous Galerkin method both horizontally and vertically. The corresponding regional dynamical core is described in Sridhar et al. (2022). For the classical high-order element-based methods, to control numerical instability produced by aliasing errors with the nonlinear terms is a difficult problem (Winters et al., 2018). To overcome this issue, a split form nodal DGM (e.g., Gassner et al., 2016) is a theoretical and computationally efficient approach. Recently, Souza et al. (2023) successfully applied one such method called "a flux-difference DGM", to a global dynamical core of dry atmosphere as the horizontal and vertical discretization. While conventional dynamical cores adopt a vertical discretization based on low-order FDM or FVM, some previous studies investigated the potential for the use of high-order vertical discretization (e.g., Guerra and Ullrich, 2016; Yi and Giraldo, 2020; Ishioka et al., 2022). For example, Guerra and Ullrich (2016) introduced an arbitrary-order vertical discretization using a staggered nodal FEM. They reported that high-order vertical discretization improves the representation of vertical dynamics at a relatively low vertical resolution.

In the current study, considering future global atmospheric simulations with O(10–100 m) grid spacing, we constructed a global nonhydrostatic atmospheric dynamical core using DGM both horizontally and vertically. For a quasi-uniform spherical grid, a cubed-sphere projection was adopted. To treat the topography, a terrain-following coordinate was used. This study includes several progresses from previous studies that developed global atmospheric dynamical cores using DGM. We focused on the following three points: 1) We attempt quantitative evaluations in a series of test cases for the global dynamical cores to reveal the impact of high-order DGM on the atmospheric flows. Few such studies for global nonhydrostatic dynamical cores are available although the numerical convergence characteristics of DGM was investigated for regional dynamical core (e.g., Giraldo and Restelli, 2008; Blaise et al., 2016). 2) The results of our study indicate that the high-order dynamical cores can provide a chance to modify the experimental setup in idealized test cases. When using the totally second-order dynamical cores, relatively large discretization errors may occur, which can overshadow the problems of ill-posed experimental setup. Fast numerical convergence achieved using high-order schemes is expected to enable detection of such problems. Even when the aim of this study goes beyond dynamical core development, we consider an evaluation framework using high-order dynamical core to be useful; For example, when new physical models are included, the physical performance can be directly evaluated by separating the effect of numerical discretization with dynamical processes. 3) Considering global LES, we formulate eddy viscous and diffusion terms in a Smagorinsky–Lilly type turbulent model in the DGM framework on the cubed-sphere coordinate. A discretization strategy for the scalar Laplacian operator on the cubed-sphere coordinate with DGM is reported in previous studies (e.g., Nair, 2009). However, they did not consider the vector Laplacian operator for the vector quantities (for example, momentum). This might be because the rigorous form of vector Laplacian is so complex that it may not be worth the computational cost required numerical stabilization. However, it is unavoidable for our purpose of introducing the turbulent model. First, using tensor analysis, we systematically derived the eddy viscosity and diffusion terms. Then, we represented the corresponding semi-discretization equations with DGM. Subsequently, a quantitative check was performed by conducting an idealized LES experiment of planetary boundary layer turbulence, which is an extension of the numerical experiments performed in KT2021 and KT2023.

The rest of this paper is organized as follows: In Sect. 2, the governing equations using the general curvilinear coordinates were formulated. Then, we introduced a cubed-sphere coordinate and a general vertical coordinate. We represented eddy viscous and diffusion terms associated with the turbulent model in the general curvilinear coordinates. Next, we explained the spatial and temporal discretization for the governing equations. In Sect. 3, we validated the proposed dynamical core through a series of idealized numerical experiments. Finally, the findings of this study and our future plans are summarized.

2 Model Description

2.1 Governing Equations

As governing equations for dry atmospheric flows, we used the three-dimensional, fully compressible nonhydrostatic equations based on the flux form (e.g., Ullrich and Jablonowski, 2012b). Following Li et al. (2020), a non-orthogonal curvilinear horizontal coordinate (ξ, η) is introduced. Subsequently, a general vertical coordinate ζ is introduced. For the horizontal coordinate transformation, the Jacobian are denoted as $\sqrt{G_h}$ and the contravariant form of the metric tensor is represented by G_h^{ij} for $i, j = 1, 2$. We define the three-dimensional metric tensor with the horizontal coordinate transformation as

$$G^{ij} = \begin{pmatrix} G_h^{11} & G_h^{12} & 0 \\ G_h^{21} & G_h^{22} & 0 \\ 0 & 0 & 1 \end{pmatrix}.$$

For the vertical coordinate transformation, the Jacobian is defined as $\sqrt{G_v} = \partial z / \partial \zeta$ and the metric tensor is defined as $G_v^{13} = \partial \zeta / \partial \xi, G_v^{23} = \partial \zeta / \partial \eta$. The vertical velocity in the transformed vertical coordinate can be written using contravariant components of wind vector (u^ξ, u^η, u^ζ) as

$$\widetilde{u^\zeta} \equiv \frac{d\zeta}{dt} = \frac{1}{\sqrt{G_v}} \left(u^\zeta + \sqrt{G_v} G_v^{13} u^\xi + \sqrt{G_v} G_v^{23} u^\eta \right).$$

The final Jacobian composed of horizontal and vertical coordinate transformations can be represented as $\sqrt{G} = \sqrt{G_h}\sqrt{G_v}$. Hereafter, to briefly describe the formulations, the coordinate variables are sometimes expressed using $(\xi_1, \xi_2, \xi_3) = (\xi, \eta, \zeta)$. In addition, the Einstein summation notation will be applied for repeated indices when representing the geometric relations.

The compact form of the governing equations can be written as

$$\frac{\partial \boldsymbol{q}}{\partial t} + \frac{\partial \left[\boldsymbol{f}(\boldsymbol{q}) + \boldsymbol{f}_{\mathrm{SGS}}(\boldsymbol{q}, \nabla \boldsymbol{q}) \right]}{\partial \xi} + \frac{\partial \left[\boldsymbol{g}(\boldsymbol{q}) + \boldsymbol{g}_{\mathrm{SGS}}(\boldsymbol{q}, \nabla \boldsymbol{q}) \right]}{\partial \eta} + \frac{\partial \left[\boldsymbol{h}(\boldsymbol{q}) + \boldsymbol{h}_{\mathrm{SGS}}(\boldsymbol{q}, \nabla \boldsymbol{q}) \right]}{\partial \zeta} = \boldsymbol{S}(\boldsymbol{q}) + \boldsymbol{S}_{\mathrm{SGS}}(\boldsymbol{q}). \tag{1}$$

Here, $\boldsymbol{q}$ is the solution vector defined as

$$\boldsymbol{q} = \left(\sqrt{G}\rho', \sqrt{G}\rho u^\xi, \sqrt{G}\rho u^\eta, \sqrt{G}\rho u^\zeta, \sqrt{G}(\rho\theta)' \right)^T, \tag{2}$$

where ρ, θ are the density and potential temperature, respectively. To treat nearly balanced flows accurately, we decomposed the density ρ and pressure p (thus $\rho\theta$) as $\phi(\xi, \eta, \zeta, t) = \phi_{\mathrm{hyd}}(\xi, \eta, \zeta) + \phi'(\xi, \eta, \zeta, t)$ where ϕ_{hyd} denotes a variable satisfying the hydrostatic balance. In Eq. (1), $\boldsymbol{f}(\boldsymbol{q})$, $\boldsymbol{g}(\boldsymbol{q})$, and $\boldsymbol{h}(\boldsymbol{q})$ are inviscid fluxes in the ξ, η, and ζ directions, respectively. The

https://doi.org/10.5194/egusphere-2024-1477
Preprint. Discussion started: 12 June 2024

horizontal inviscid fluxes are represented as

$$\boldsymbol{f}(\boldsymbol{q}) = \begin{pmatrix} \sqrt{G}\rho u^{\xi} \\ \sqrt{G}(\rho u^{\xi}u^{\xi} + G_h^{11}p') \\ \sqrt{G}(\rho u^{\eta}u^{\xi} + G_h^{21}p') \\ \sqrt{G}\rho u^{\zeta}u^{\xi} \\ \sqrt{G}\rho\theta u^{\xi} \end{pmatrix}, \quad \boldsymbol{g}(\boldsymbol{q}) = \begin{pmatrix} \sqrt{G}\rho u^{\eta} \\ \sqrt{G}(\rho u^{\xi}u^{\eta} + G_h^{12}p') \\ \sqrt{G}(\rho u^{\eta}u^{\eta} + G_h^{22}p') \\ \sqrt{G}\rho u^{\zeta}u^{\eta} \\ \sqrt{G}\rho\theta u^{\eta} \end{pmatrix}, \tag{3}$$

and the vertical inviscid fluxes are represented as

$$\boldsymbol{h}(\boldsymbol{q}) = \begin{pmatrix} \sqrt{G}\rho\widetilde{u^{\zeta}} \\ \sqrt{G}[\rho u^{\xi}\widetilde{u^{\zeta}} + (G_v^{13}G_h^{11} + G_v^{23}G_h^{12})p'] \\ \sqrt{G}[\rho u^{\eta}\widetilde{u^{\zeta}} + (G_v^{13}G_h^{21} + G_v^{23}G_h^{22})p'] \\ \sqrt{G}\rho u^{\zeta}\widetilde{u^{\zeta}} + \sqrt{G}_h p' \\ \sqrt{G}\rho\theta\widetilde{u^{\zeta}} \end{pmatrix}. \tag{4}$$

Furthermore, $\boldsymbol{S}(\boldsymbol{q})$ represents the source terms as

$$\boldsymbol{S}(\boldsymbol{q}) = \begin{pmatrix} 0 \\ \sqrt{G}(F_H^1 + F_M^1 + F_C^1) \\ \sqrt{G}(F_H^2 + F_M^2 + F_C^2) \\ \sqrt{G}(F_{\mathrm{buo}} + F_C^3) \\ 0 \end{pmatrix},$$

where F_H^i for $i = 1,2$ are the horizontal pressure gradient terms with hydrostatic balance and can be written as

$$F_H^i = -\frac{G_h^{im'}}{\sqrt{G_v}}\left[\frac{\partial(\sqrt{G_v}p_{\mathrm{hyd}})}{\partial\xi^{m'}} + \frac{\partial(G_v^{m'3}\sqrt{G_v}p_{\mathrm{hyd}})}{\partial\xi^3}\right],$$

here, note that $m' = 1,2$; $F_M^i = -\Gamma_{ml}^i(\rho u^m u^l + G^{ml}p')$ are the source terms due to the horizontal curvilinear coordinate, where m,l are $1,2,3$ and Γ_{ml}^i is the Christoffel symbol of the second kind, which means the spatial variation of basis vector; $F_C^i = -G^{im}\epsilon_{jml}2\Omega^m\rho u^l$ are the Coriolis terms, where ϵ_{jkl} is the three rank Levi–Civita tensor and Ω^k are the components of angular velocity vector; $F_{\mathrm{buo}} = -\rho'(a/r)^2 g$ is the buoyancy term, where r is the radial coordinate, a is the planetary radius, and g is the standard gravitational acceleration. To close the equation systems, the pressure p is calculated using the state equation for the ideal gas as

$$p = P_0\left(\frac{R}{P_0}\rho\theta\right)^{\frac{C_p}{C_v}},$$

where P_0 is a constant pressure, R is the gas constant, and C_v and C_p are the specific heat at constant volume and constant pressure, respectively. The actual values for the constants mentioned above is provided in Table 1. In Eq. (1), the terms with subscript SGS are associated with a turbulent model; $\boldsymbol{f}_{\mathrm{SGS}}(\boldsymbol{q},\nabla\boldsymbol{q})$, $\boldsymbol{g}_{\mathrm{SGS}}(\boldsymbol{q},\nabla\boldsymbol{q})$, and $\boldsymbol{h}_{\mathrm{SGS}}(\boldsymbol{q},\nabla\boldsymbol{q})$ are the parameterized eddy fluxes while $\boldsymbol{S}_{\mathrm{SGS}}(\boldsymbol{q}, \nabla \boldsymbol{q})$ are the source terms with the curvilinear coordinate. The terms associated with the turbulent model are detailed in Sect. 2.2.

As a horizontal curvilinear coordinate, an equiangular gnomonic cubed-sphere projection (Sadourny, 1972; Ronchi et al., 1996) was adopted to map a cube onto a sphere. Compared to a conformal projection (Rančić et al., 1996), we preferred this projection to generate more uniform grids in high spatial resolutions, although non-orthogonal basis need to be treated. In each panel of the cube, a local coordinate using the central angles (α, β) $(\in [-\pi/4, \pi/4])$ is introduced and related to the horizontal coordinates (ξ, η) by $\xi = \alpha, \eta = \beta$. For the equiangular gnomonic cubed-sphere projection, we denote the horizontal contravariant metric tensor and the Jacobian as G_c and $\sqrt{G_c}$, respectively. Based on the derivation with the coordinate transformation in previous studies (e.g., Nair et al., 2005; Ullrich et al., 2012; Li et al., 2020), G_c and $\sqrt{G_c}$ are analytically obtained as

$$G_c^{ij} = \frac{\delta^2}{r^2(1+X^2)(1+Y^2)} \begin{pmatrix} 1+Y^2 & XY \\ XY & 1+X^2 \end{pmatrix}, \quad \sqrt{G_c} = \frac{r^2(1+X^2)(1+Y^2)}{\delta^3}, \tag{5}$$

where $X = \tan\alpha$, $Y = \tan\beta$, $\delta = \sqrt{1+X^2+Y^2}$, and r is the radial coordinate. The Christoffel symbol of the second kind Γ^i_{ml} is written as

$$\Gamma^1_{ml} = \begin{pmatrix} \frac{2XY^2}{\delta^2} & \frac{-Y(1+Y^2)}{\delta^2} & \frac{\delta_S}{r} \\ \frac{-Y(1+Y^2)}{\delta^2} & 0 & 0 \\ \frac{\delta_S}{r} & 0 & 0 \end{pmatrix}, \quad \Gamma^2_{ml} = \begin{pmatrix} 0 & \frac{-X(1+X^2)}{\delta^2} & 0 \\ \frac{-X(1+X^2)}{\delta^2} & \frac{2X^2Y}{\delta^2} & \frac{\delta_S}{r} \\ 0 & \frac{\delta_S}{r} & 0 \end{pmatrix},$$

$$\Gamma^3_{ml} = \delta_S \frac{r(1+X^2)(1+Y^2)}{\delta^4} \begin{pmatrix} -(1+X^2) & XY & 0 \\ XY & -(1+Y^2) & 0 \\ 0 & 0 & 0 \end{pmatrix}, \tag{6}$$

where δ_S is an index for shallow atmosphere approximation. The components of angular velocity vector included in the Coriolis terms F^i_C are given as

$$\Omega^1 = 0, \quad \Omega^2 = \delta_S \frac{\omega\delta}{r(1+Y^2)}, \quad \Omega^3 = \omega\frac{Y}{\delta}, \qquad \text{for the equatorial panels,}$$

$$\Omega^1 = -\delta_S \frac{s\omega X\delta}{r(1+X^2)}, \quad \Omega^2 = -\delta_S \frac{s\omega Y\delta}{r(1+Y^2)}, \quad \Omega^3 = \frac{s\omega}{\delta}, \qquad \text{for the polar panels,} \tag{7}$$

where ω is the angular velocity of planet; We introduced an index s with a value of 1 and -1 for the Northern and Southern polar panels, respectively. In numerical experiments in Sect. 3, the shallow atmosphere approximation was applied. Then, r and δ_S were treated as follows: the radial coordinate r in Eqs. (5)–(7) and the buoyancy term in Eq. (4) is replaced by the planetary radius a. In Eqs. (6) and (7), the terms with δ_S are ignored. In addition, the pressure contribution in F^i_M disappears since a relation of $\Gamma^i_{ml} G^{ml} = 0$ is satisfied in the shallow atmosphere approximation.

To treat the topography, in this study, we adopted the traditional terrain-following coordinate (Phillips, 1957; Gal-Chen and Somerville, 1975) as a general vertical coordinate. The vertical coordinate conversion is defined as

$$\zeta = z_T \frac{z-h}{z_T-h},$$

where z is the height coordinate, z_T is the top height of computational domain (we assume it is a constant value) and h is the surface height. The corresponding Jacobian and metric tensor can be written as

$$\sqrt{G_v} = 1 - \frac{h}{z_T}, \quad \sqrt{G_v}G_v^{13} = \left(\frac{\zeta}{z_T} - 1\right)\frac{\partial h}{\partial \xi}, \quad \sqrt{G_v}G_v^{23} = \left(\frac{\zeta}{z_T} - 1\right)\frac{\partial h}{\partial \eta},$$

respectively.

2.2 Formulation of eddy viscous and diffusion terms in general curvilinear coordinates

Considering global LES in future high-resolution simulations, this subsection describes eddy viscous and diffusion terms in the general curvilinear coordinates. We focus on a Smagorinsky–Lilly type model (Smagorinsky, 1963; Lilly, 1962) considered the stratification effect (Brown et al., 1994), which was used in our previous studies (KT2021 and KT2023). The Favre-filtering (Favre, 1983) was used as a spatial filter. We did not explicitly denote the symbol representing the spatial filter because the filtering approach is essentially same as that explained in Appendix A of KT2023. The difficulties in the derivation of viscous and diffusion terms are caused by the gradient of vector quantities and the spatial divergence with the non-orthogonal basis because the manipulations become increasingly complex. However, previous studies that utilized tensor analysis help us provide a systematic derivation (e.g., Rančić et al., 2017). In the absence of vertical coordinate transformation, the parameterized fluxes with the turbulent model can be represented in the general curvilinear coordinates as

$$\boldsymbol{f}_{\mathrm{SGS}}(\boldsymbol{q}, \nabla \boldsymbol{q}) = \begin{pmatrix} 0 \\ -\sqrt{G}\rho\tau^{11} \\ -\sqrt{G}\rho\tau^{12} \\ -\sqrt{G}\rho\tau^{13} \\ -\sqrt{G}\rho\tau_*^{1} \end{pmatrix}, \quad \boldsymbol{g}_{\mathrm{SGS}}(\boldsymbol{q}, \nabla \boldsymbol{q}) = \begin{pmatrix} 0 \\ -\sqrt{G}\rho\tau^{21} \\ -\sqrt{G}\rho\tau^{22} \\ -\sqrt{G}\rho\tau^{23} \\ -\sqrt{G}\rho\tau_*^{2} \end{pmatrix}, \quad \boldsymbol{h}_{\mathrm{SGS}}(\boldsymbol{q}, \nabla \boldsymbol{q}) = \begin{pmatrix} 0 \\ -\sqrt{G}\rho\tau^{31} \\ -\sqrt{G}\rho\tau^{32} \\ -\sqrt{G}\rho\tau^{33} \\ -\sqrt{G}\rho\tau_*^{3} \end{pmatrix},$$

and the source term is

$$\boldsymbol{S}_{\mathrm{SGS}}(\boldsymbol{q}, \nabla \boldsymbol{q}) = \begin{pmatrix} 0 \\ -\sqrt{G}\Gamma^1_{ml}\rho\tau^{ml} \\ -\sqrt{G}\Gamma^2_{ml}\rho\tau^{ml} \\ -\sqrt{G}\Gamma^3_{ml}\rho\tau^{ml} \\ 0 \end{pmatrix}.$$

In the equations, τ^{ij} is the contravariant components of parameterized eddy viscous flux tensor ($i = 1,2,3$ and $j = 1,2,3$) and can be written as

$$\tau^{ij} = -2\nu_{\mathrm{SGS}}\left(S^{ij} - \frac{G^{ij}}{3}D\right) - \frac{2}{3}G^{ij}K_{\mathrm{SGS}},$$

where S^{ij} is the strain velocity tensor, ν_{SGS} is the eddy viscosity, D is the divergence of three-dimensional velocity, and K_{SGS} is the SGS kinetic energy. The strain velocity tensor is represented as

$$S^{ij} = \frac{1}{2}\left(G^{im}\frac{\partial u^j_{,m}}{\partial \xi^m} + G^{jm}\frac{\partial u^i_{,m}}{\partial \xi^m}\right),$$

https://doi.org/10.5194/egusphere-2024-1477
Preprint. Discussion started: 12 June 2024

using the covariant derivative of the contravariant component

$$u^i_{,j} = \frac{\partial u^i}{\partial \xi^j} + u^m \Gamma^i_{jm}.$$

The eddy viscosity is written as

$$\nu_{\mathrm{SGS}} = C_s \Delta_{\mathrm{SGS}} |S|,$$

where C_s, Δ_{SGS}, and $|S|$ represent the Smagorinsky constant, the filter length, and the norm of strain tensor defined as $\sqrt{2G_{im}G_{jn}S^{ij}S^{mn}}$, respectively. The parameterized eddy diffusive flux can be written as

$$\tau^i_* = -\nu^*_{\mathrm{SGS}} G^{ij} \frac{\partial \theta}{\partial \xi^j},$$

where ν^*_{SGS} is the eddy diffusion coefficient. For further details of turbulent model, refer to Sect. 2.2 of Nishizawa et al. (2015).

2.3 Spatial discretization

The spatial discretization for Eq. (1) is based on a nodal DGM (e.g., Hesthaven and Warburton, 2007). In each cubed-sphere panel, the three-dimensional computational domain Ω is divided using non-overlapping hexahedral elements. To relate the coordinates $(\xi^1, \xi^2, \xi^3) = (\alpha, \beta, \zeta)$ with the local coordinates $\tilde{\boldsymbol{x}} \equiv (\tilde{x}^1, \tilde{x}^2, \tilde{x}^3)$ in a reference element Ω_e, we adopted a linear mapping defined as

$$\tilde{x}^i = 2\frac{\xi^i - \xi^i_e}{h^i_e}, \tag{8}$$

where ξ^i_e and h^i_e represent the center position and width of the element in the ξ^i-direction, respectively. By equally dividing the (α, β) plane, we generate a horizontal mesh including $N_{e,h} \times N_{e,h}$ finite elements. The center horizontal position of (i', j')-th element is given by

$$\alpha_{i'} = -\frac{\pi}{4} + \frac{\pi}{2N_{e,h}}\left(i' - \frac{1}{2}\right), \quad \beta_{j'} = -\frac{\pi}{4} + \frac{\pi}{2N_{e,h}}\left(j' - \frac{1}{2}\right).$$

Using the tensor-product of one-dimensional Lagrange polynomials $l_{\boldsymbol{m}}(\tilde{\boldsymbol{x}}) = l_{m_1}(\tilde{x}^1) l_{m_2}(\tilde{x}^2) l_{m_3}(\tilde{x}^3)$, a local approximated solution within each element Ω_e is represented as

$$\boldsymbol{q}^e|_{\Omega_e}(\tilde{\boldsymbol{x}}, t) = \sum_{m_1=1}^{p+1} \sum_{m_2=1}^{p+1} \sum_{m_3=1}^{p+1} \boldsymbol{Q}^e_{m_1,m_2,m_3}(t)\ \ l_{m_1}(\tilde{x}^1) l_{m_2}(\tilde{x}^2) l_{m_3}(\tilde{x}^3), \tag{9}$$

In Eq. (9), the coefficients $Q^e_{m_1,m_2,m_3}$ are the unknown degrees of freedom (DOF) and p is the polynomial order. In this study, the Legendre–Gauss–Lobatto (LGL) points were used for interpolation and integration nodes. We defined an effective horizontal grid spacing at the equator as

$$\Delta_{h,\mathrm{eq}} = \frac{\pi a}{2N_{e,h}(p+1)},$$

which approximately corresponds to the grid spacing in the grid-point methods.

By applying the Galerkin approximation to Eq. (1), we obtain a strong form of the semi-discretized equations as

$$\begin{aligned}\frac{d}{dt}\int_{\Omega_e} \boldsymbol{q}^e(\tilde{\boldsymbol{x}},t)\, l_{\boldsymbol{m}}(\tilde{\boldsymbol{x}})\, J^E\, d\tilde{\boldsymbol{x}} = &-\sum_{j=1}^{3}\int_{\Omega_e} \frac{\partial \boldsymbol{F}_j(\boldsymbol{q}^e,\boldsymbol{G})}{\partial \xi^j} l_{\boldsymbol{m}}(\tilde{\boldsymbol{x}})\, J^E\, d\tilde{\boldsymbol{x}} \\ &-\int_{\partial\Omega_e} \left[\hat{\boldsymbol{F}}(\boldsymbol{q}^e,\boldsymbol{G}) - \boldsymbol{F}(\boldsymbol{q}^e,\boldsymbol{G})\right]\cdot \boldsymbol{n}\, l_{\boldsymbol{m}}(\tilde{\boldsymbol{x}})\, J^{\partial E}\, dS \\ &+\int_{\Omega_e} \left[\boldsymbol{S}(\boldsymbol{q}^e) + \boldsymbol{S}_{\mathrm{SGS}}(\boldsymbol{q}^e,\boldsymbol{G})\right] l_{\boldsymbol{m}}(\tilde{\boldsymbol{x}})\, J^E\, d\tilde{\boldsymbol{x}},\end{aligned} \tag{10}$$

where $(\boldsymbol{F}_1,\boldsymbol{F}_2,\boldsymbol{F}_3) = (\boldsymbol{f}+\boldsymbol{f}_{\mathrm{SGS}}, \boldsymbol{g}+\boldsymbol{g}_{\mathrm{SGS}}, \boldsymbol{h}+\boldsymbol{h}_{\mathrm{SGS}})$ is the flux vector tensor, $\hat{\boldsymbol{F}}$ is the numerical flux at the element boundary $\partial\Omega_E$, and $\boldsymbol{n}$ is the outward unit vector normal to $\partial\Omega_E$; In the volume and surface integrals, J^E and $J^{\partial E}$ represent the transformation Jacobian with the general curvilinear coordinates and local coordinates within each element. Note that, because of the linear mapping in Eq. (8), the associated geometric factors such as J^E and $J^{\partial E}$ have a constant value in when the volume and surface integrals are calculated. For the turbulent model, we need to evaluate the eddy viscous flux tensor and diffusion flux, which include a few gradient terms with quantities such as $\chi = (u^\xi, u^\eta, u^\zeta, \theta)$, denoted by $\boldsymbol{G} = (\partial\chi/\partial\xi^1, \partial\chi/\partial\xi^2, \partial\chi/\partial\xi^3)$ in Eq. (10). The gradient discretization in the ξ^j-direction is given by

$$\begin{aligned}\int_{\Omega_e} \rho\, \boldsymbol{G}_j l_{\boldsymbol{m}}(\tilde{\boldsymbol{x}})\, J^E\, d\tilde{\boldsymbol{x}} = &\int_{\Omega_e} \left[\frac{\partial \rho^e \chi^e}{\partial \xi^j} - \chi^e \left(\frac{\partial \rho}{\partial \xi^j}\right)^e\right] l_{\boldsymbol{m}}(\tilde{\boldsymbol{x}})\, J^E\, d\tilde{\boldsymbol{x}} \\ &+\int_{\partial\Omega_e} (\widehat{\rho\chi} - \rho^e\chi^e)\, \boldsymbol{n}_{\tilde{x}^j}\cdot \boldsymbol{n}\, l_{\boldsymbol{m}}(\tilde{\boldsymbol{x}})\, J^{\partial E}\, dS,\end{aligned} \tag{11}$$

where $\boldsymbol{n}_{\tilde{\boldsymbol{x}}^j}$ is the unit vector in the $\tilde{x}^j$-direction and the density gradient is calculated by

$$\int_{\Omega_e} \left(\frac{\partial \rho}{\partial \xi^j}\right)^e l_{\boldsymbol{m}}(\tilde{\boldsymbol{x}})\, J^E\, d\tilde{\boldsymbol{x}} = \int_{\Omega_e} \frac{\partial \rho^e}{\partial \xi^j} l_{\boldsymbol{m}}(\tilde{\boldsymbol{x}})\, J^E\, d\tilde{\boldsymbol{x}} + \int_{\partial\Omega_e} (\hat{\rho} - \rho^e)\, \boldsymbol{n}_{\tilde{x}^j}\cdot \boldsymbol{n}\, l_{\boldsymbol{m}}(\tilde{\boldsymbol{x}})\, J^{\partial E}\, dS.$$

For the numerical flux of inviscid terms, this study used the Rusanov flux (Rusanov, 1961) as a simple choice of the approximated Riemann solvers. Its numerical dissipation is provided based on the maximum absolute eigenvalue of the Jacobian matrix at the left and right sides of the element boundary. From previous studies (Li et al., 2020), the Rusanov flux considered the horizontal and vertical coordinate transformations is formulated as

$$\hat{\boldsymbol{F}}_{\mathrm{invis}} = \frac{1}{2}\left\{\left[\boldsymbol{F}_{\mathrm{invis}}(\boldsymbol{q}^+) + \boldsymbol{F}_{\mathrm{invis}}(\boldsymbol{q}^-)\right]\cdot \boldsymbol{n} - \lambda_{\max}\left[\boldsymbol{q}^+ - \boldsymbol{q}^-\right]\right\},$$

where $\lambda_{\max}$ is the maximum of the absolute value of eigenvalues of the flux Jacobian in the direction $\boldsymbol{n}$, and $\boldsymbol{q}^-$ and $\boldsymbol{q}^+$ represent the interior and exterior values at $\partial\Omega_e$. At the element boundaries in the horizontal directions (ξ and η), $\lambda_{\max}$ can be represented as

$$\lambda_{\max,\xi} = \left|u^\xi\right| + \sqrt{G_c^{11}}\, c_s, \quad \lambda_{\max,\eta} = |u^\eta| + \sqrt{G_c^{22}}\, c_s,$$

respectively, where $c_s = [(C_p/C_v)RT]^{1/2}$ is the speed of sound wave. For the vertical direction ζ, $\lambda_{\max}$ can be represented as

$$\lambda_{\max,\zeta} = \left|\widetilde{u^{\zeta}}\right| + \left[1/\sqrt{G_v} + G_v^{13}G_X + G_v^{23}G_Y\right]^{1/2} c_s,$$

where $G_X = G_v^{13}G_c^{11} + G_v^{23}G_c^{12}$ and $G_Y = G_v^{13}G_c^{21} + G_v^{23}G_c^{22}$. As the numerical flux of the gradient $\boldsymbol{G}$ and the SGS fluxes $(\boldsymbol{f}_{\mathrm{SGS}}, \boldsymbol{g}_{\mathrm{SGS}}, \boldsymbol{h}_{\mathrm{SGS}})$ with the turbulent model, we adopted the central flux.

When the same nodes are used for interpolation and integration (i.e., collocation), we can obtain a matrix form of Eqs. (10) and (11) as

$$\frac{d\boldsymbol{q}^e}{dt} = -\sum_{j=1}^{3} d_j D_{\tilde{x}^j} \boldsymbol{F}_j(\boldsymbol{q}^e, \boldsymbol{G}) - \sum_{f=1}^{6} s_{\partial\Omega_{e,f}} L_{\partial\Omega_{e,f}} \left[\hat{\boldsymbol{F}}(\boldsymbol{q}^e, \boldsymbol{G}) - \boldsymbol{F}(\boldsymbol{q}^e, \boldsymbol{G})\right] \cdot \boldsymbol{n}$$
$$+ \boldsymbol{S}(\boldsymbol{q}^e) + \boldsymbol{S}_{\mathrm{SGS}}(\boldsymbol{q}^e, \boldsymbol{G}), \tag{12}$$

$$\rho\, \boldsymbol{G}_j = d_j D_{\tilde{x}^j}(\rho^e \boldsymbol{\chi}^e) - \boldsymbol{\chi}^e \left(\frac{\partial \rho}{\partial \xi^j}\right)^e + \sum_{f'=1}^{2} s_{\partial\Omega_{e,f'}} L_{\partial\Omega_{e,f'}} \left(\widehat{\rho\boldsymbol{\chi}} - \rho^e \boldsymbol{\chi}^e\right) \boldsymbol{n}_{\tilde{x}^j} \cdot \boldsymbol{n}, \tag{13}$$

where $D_{\tilde{x}^j}$ represents the differential matrix for the $\tilde{x}^j$-direction; $L_{\partial\Omega_{e,f}}$ represents the lifting matrix with the surface integral for the f-th element surface, and $L_{\partial\Omega_{e,f'}}$ represent the same for the f'-th element surface in the gradient operator for the $\tilde{x}^j$-direction. The components of these matrices are given as

$$(D_{\tilde{x}^j})_{\boldsymbol{m},\boldsymbol{m}'} = M^{-1} \int_{\Omega_e} l_{\boldsymbol{m}} \frac{\partial l_{\boldsymbol{m}'}}{\partial \tilde{x}_j}\, d\tilde{\boldsymbol{x}}, \quad (L_{\partial\Omega_e,j})_{\boldsymbol{m},\boldsymbol{m}'} = M^{-1} \int_{\partial\Omega_{e,j}} l_{\boldsymbol{m}} l_{\boldsymbol{m}'}^{\partial\Omega_{e,j}}\, dS, \tag{14}$$

where M denotes the mass matrix given by

$$M_{\boldsymbol{m},\boldsymbol{m}'} = \int_{\Omega_e} l_{\boldsymbol{m}} l_{\boldsymbol{m}'}\, d\tilde{\boldsymbol{x}}. \tag{15}$$

The density gradient term is calculated by

$$\left(\frac{\partial \rho}{\partial \xi^j}\right)^e = d_j D_{\tilde{x}^j} \rho^e - \sum_{f'=1}^{2} s_{\partial\Omega_{e,f'}} L_{\partial\Omega_{e,f'}} (\widehat{\rho} - \rho^e)\, \boldsymbol{n}_{\tilde{x}^j} \cdot \boldsymbol{n}. \tag{16}$$

Note that, in Eqs. (12), (13), and (16), $d_j = \partial\tilde{x}^j/\partial\xi^j$ and $s_{\partial\Omega_{e,j}} = J_{\partial\Omega_{e,j}}/J^E$ are constant values in the volume and surface integrals, respectively. We changed the calculation method of mass and lifting matrices depending on temporal discretization; This is detailed in Sect. 2.4.

The balance between the pressure gradient and buoyancy terms should be carefully treated in the discrete momentum equation (e.g., Blaise et al., 2016; Orgis et al., 2017). Because a different discretization space is used between the terms in the above formulation, a numerical imbalance is possible and may cause spurious oscillations, which can destabilize the simulations. To avoid this incompatibility, the vertical polynomial order for the density in the buoyancy term was reduced by one following Blaise et al. (2016).

2.4 Temporal discretization

The semi-discretized equations in Eq. (10) can be represented as an ordinary differential equation (ODE) system as

$$\frac{d\boldsymbol{q}}{dt} = \mathcal{S}(\boldsymbol{q}, \nabla \boldsymbol{q}) + \mathcal{F}(\boldsymbol{q}, \nabla \boldsymbol{q}), \tag{17}$$

where $\mathcal{S}(\boldsymbol{q}, \nabla \boldsymbol{q})$ and $\mathcal{F}(\boldsymbol{q}, \nabla \boldsymbol{q})$ represent the tendencies with slow and fast contributions, respectively. This study adopted Runge–Kutta (RK) schemes to solve the ODE system from $t = n\Delta t$ to $t = (n+1)\Delta t$, where Δt is the time step and n is a natural number. In this subsection, we describe two approaches for temporal discretization, namely, horizontal explicit and vertical implicit (HEVI) and horizontal explicit and vertical explicit (HEVE) approaches.

2.4.1 HEVI approach

If the aspect ratio of horizontal grid spacing to its vertical counterpart is large, it is impractical to use fully explicit temporal schemes because the vertically propagating sound waves severely restrict to the timestep. A strategy to avoid computational cost in such case is the HEVI approach. The terms corresponding to vertical dynamics with a fast time-scale are evaluated using an implicit temporal scheme, while the remaining terms are evaluated using an explicit temporal scheme. Such procedure can be regarded as a framework of implicit-explicit (IMEX) time integration scheme (Bao et al., 2015; Gardner et al., 2018). General formulation of IMEX RK scheme (e.g., Ascher et al., 1997) with ν stages can be written as

$$\begin{aligned}
\boldsymbol{q}^{(s)} &= \boldsymbol{q}^n + \Delta t \sum_{s'=1}^{s-1} a_{ss'} \mathcal{S}(t + c_{s'}\Delta t, \boldsymbol{q}^{(s')}) + \Delta t \sum_{s'=1}^{s} \tilde{a}_{ss'} \mathcal{F}(t + \tilde{c}_{s'}\Delta t, \boldsymbol{q}^{(s')}) \quad \text{for} \quad s = 1, \ldots, \nu \\
\boldsymbol{q}^{n+1} &= \boldsymbol{q}^n + \Delta t \sum_{s=1}^{\nu} b_s \mathcal{S}(t + c_s\Delta t, \boldsymbol{q}^{(s)}) + \Delta t \sum_{s=1}^{\nu} \tilde{b}_s \mathcal{F}(t + \tilde{c}_s\Delta t, \boldsymbol{q}^{(s)}),
\end{aligned}$$

where $a_{ss'}$, b_s, and c_s define the explicit temporal integrator, while $\tilde{a}_{ss'}$, $\tilde{b}_s$, and $\tilde{c}_{s'}$ define the implicit temporal integrator; $c_s = \sum_{s'=1}^{s-1} a_{ss'}$ and $\tilde{c}_s = \sum_{s'=1}^{s-1} \tilde{a}_{ss'}$ represents time when slow and fast terms are evaluated, respectively. These coefficients are compactly represented using "double Butcher tableaux", as shown in Table 2. Note that, in the table of the explicit part, $\mathscr{A} = \{a_{ss'}\}$ with $a_{ss'} = 0$ for $s' \geq s$. On the other hand, for the implicit part, $\tilde{\mathscr{A}} = \{\tilde{a}_{ss'}\}$ with $\tilde{a}_{ss'} = 0$ for $s' > s$ in case of the diagonally implicit RK scheme.

In this study, the terms associated with vertical mass flux, vertical pressure gradient, vertical flux of potential temperature, and buoyancy in Eqs. (1) are treated as fast terms, whereas the other terms are treated as slow terms. To minimize contaminating the spatial accuracy of high-order DGM by temporal errors with low-order HEVI scheme, this study adopted a third-order scheme proposed by Kennedy and Carpenter (2003); it includes four explicit and three implicit evaluations. The corresponding double Butcher tableaux are given in Table 2. In the implicit part of each stage, the corresponding nonlinear equation system was solved using Newton's method. In each iteration, the linearized equation system is solved. To obtain the solutions of nonlinear equation system precisely, we need a lot of iterations. However, this study performed a single iteration in Newton's method (i.e., Rosenbrock approach), thus reducing the computational cost significantly. Such approach has been used in previous studies (e.g., Ullrich and Jablonowski, 2012a). In the case of collocation approach, because the horizontal dependency between all nodes within the element vanishes, the vertical implicit evaluation can be parallelly performed at each horizontal node.

For the case of HEVI, we evaluated the volume and surface integrations in Eqs. (14) and (15) using inexact integration with the LGL nodes. Consequently, $\boldsymbol{M}$ and $\boldsymbol{L}_{\partial\Omega_{e,3}}$ become diagonal matrices, which further simplify the matrix structure associated with the vertical spatial operator.

2.4.2 HEVE approach

When we consider a horizontal grid spacing with O(10 m) such as in LES, the ratio of horizontal to vertical grid spacing approaches unity. The advantages of HEVI approach decrease. Thus, it is suitable to adopt a fully explicit temporal approach, referred to as HEVE approach. In such cases, RK schemes with strong stability preserving (SSP) property (e.g., Gottlieb et al., 2001) are often used together with DGM. Same as in KT2023, this study adopted a ten-stage RK scheme with the fourth-order accuracy proposed by Ketcheson (2008). The corresponding Butcher table is given in Table 3. When using HEVE approach, entries of matrices in Eqs. (14) and (15) were directly calculated following Sect. 3.2 in Hesthaven and Warburton (2007).

2.5 Modal filtering

For high-order methods, numerical instability is likely to occur because inherent numerical dissipations are small. Further, we adopted a collocation approach due to its computational efficiency as described in Sect. 2.3. One drawback is that the aliasing errors with evaluations of the nonlinear terms can drive numerical instability. To suppress the numerical instability, a modal filter was used as an additional stabilization mechanism. The filter matrix for the three-dimensional problem can be obtained as

$$\mathscr{F} = V^{3\mathrm{D}} C^{3\mathrm{D}} V^{3\mathrm{D}},$$

where $V^{3\mathrm{D}}$ represents the Vandermode matrix associated with the LGL interpolation nodes (in Eq. (9)) and $C^{3\mathrm{D}}$ represents is the diagonal cutoff matrix. The entries of $C^{3\mathrm{D}}$ are defined as

$$C^{3\mathrm{D}}_{(m_1,m_2,m_3),(m_1',m_2',m_3')} = \delta_{m_1,m_1'}\sigma^h_{m_1}\ \delta_{m_2,m_2'}\sigma^h_{m_2}\ \delta_{m_3,m_3'}\sigma^v_{m_3},$$

where σ^h_i represents the decay coefficient for the one-dimensional horizontal mode i, while σ^v_i represents that for the vertical mode i. Based on Hesthaven and Warburton (2007), a typical choice of the coefficient for mode i is provided with an exponential function as

$$\sigma_i = \begin{cases} 1 & \text{if } 0 \le i \le p_c \\ \exp\left[-\alpha_i \left(\dfrac{i-p_c}{p-p_c}\right)^{p_m}\right] & \text{if } p_c \le i \le p, \end{cases} \tag{18}$$

where p_c, p_m, and α_i represent the cutoff parameter ($p_c = 0$ in this study), the order of filter, and the non-dimensional decay strength, respectively. We applied the filter $\mathscr{F}$ to the solution vector $\boldsymbol{q}$ (in Eq. (2)) at the final stage of RK scheme with a timestep Δt. Then, the decay time scale for the highest mode is regarded as approximately equal to $\Delta t/\alpha_m$.

https://doi.org/10.5194/egusphere-2024-1477
Preprint. Discussion started: 12 June 2024

3 Validation of dynamical core

To validate our dynamical core, we conducted several tests, which are summarized in Table. 1. When evaluating numerical errors for the deterministic experiments such as linear advection, gravity wave, mountain wave, and baroclinic wave tests, we use the following error norms as

$$L_{1,\mathrm{error}} = \frac{\sum_E \int_{\Omega_E} |\psi(\xi,\eta,\zeta,t) - \psi_{\mathrm{ref}}(\xi,\eta,\zeta,t)|\,\mathrm{d}\boldsymbol{x}}{\sum_E \int_{\Omega_E} \mathrm{d}\boldsymbol{x}},$$

$$L_{2,\mathrm{error}} = \left[\frac{\sum_E \int_{\Omega_E} [\psi(\xi,\eta,\zeta,t) - \psi_{\mathrm{ref}}(\xi,\eta,\zeta,t)]^2\,\mathrm{d}\boldsymbol{x}}{\sum_E \int_{\Omega_E} \mathrm{d}\boldsymbol{x}}\right]^{1/2},$$

$$L_{\mathrm{inf,error}} = \max\left[\psi(\xi,\eta,\zeta,t) - \psi_{\mathrm{ref}}(\xi,\eta,\zeta,t)\right],$$

where $\psi(\xi,\eta,\zeta,t)$ and $\psi_{\mathrm{ref}}(\xi,\eta,\zeta,t)$ denote the numerical and reference solutions, respectively, and $\sum_E$ represents the summation over all elements. Except for the linear advection test case, the results obtained from a sufficiently high-resolution experiment were used as the reference solution since the exact solution is unknown. In such case, the numerical solution was interpolated into the computational grid with the highest resolution experiment when evaluating the error norms.

For idealized climatological or turbulent flow simulations such as the Held Suarez and global LES tests, it is difficult to directly evaluate the numerical convergence. Thus, we mainly investigated on the impact of polynomial order on effective resolution while focusing on the energy spectra.

3.1 Linear advection

To validate the spatial discretization with the cubed-sphere geometry, we conducted a test for two-dimensional linear advection of a scalar quantity q. The experimental setup is similar to test case 1 of Williamson et al. (1992). The longitudinal and latitudinal components of horizontal wind are prescribed by a solid body rotation as

$$u = u_0(\cos\theta\cos\alpha + \sin\theta\cos\lambda\sin\alpha), \quad v = -u_0\sin\lambda\sin\alpha,$$

where λ and θ are the longitude and latitude coordinates, respectively, $u_0 = 2\pi a/(12[\mathrm{days}])$, and α denotes the angle between the axis of solid body rotation and the North pole. We considered three values of $\alpha = 0, \pi/4, \pi/2$ radians to investigate the impact of singularity with four corners of each panel in the cubed sphere. Although a cosine-bell profile is often given as an initial profile of the advected field, a Gaussian profile was used in this test case to ensure the order of accuracy is higher than two. The profile is defined as

$$q(\lambda,\theta) = \exp\left(-\frac{d(\lambda,\theta)}{D}\right),$$

where D is the characteristic horizontal scale; d is the great circle distance between a position on the sphere (λ,θ) and the center position of Gaussian profile (λ_c,θ_c), which is calculated by

$$d(\lambda,\theta) = a\arccos\left[\sin\theta_c\sin\theta + \cos\theta_c\cos\theta\cos(\lambda-\lambda_c)\right]. \tag{19}$$

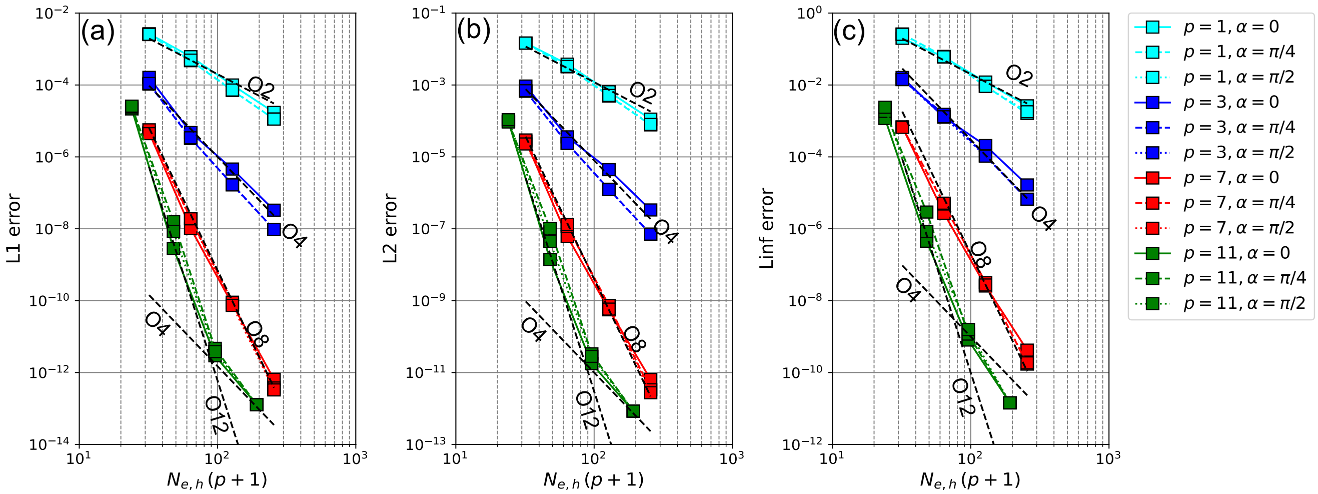

Figure 1. Dependence of (a) L_1, (b) L_2, and (c) L_{inf} errors at $t = 12$ days on horizontal resolution in a two-dimensional linear advection problem using $p = 1$, 3, 7, and 11. The colored solid, dashed, and dotted lines represent the results for $\alpha = 0$, $\pi/4$, and $\pi/2$, respectively. A black dashed line labeled "O*n*" indicates the slope with *n*-th order accuracy.

In this experiment, we set to $D = a/5$ and $(\lambda_c, \theta_c) = (3\pi/2, 0)$.

To investigate a convergence rate of numerical solutions, we changed the horizontal resolution as $N_{e,h}(p+1) = 32, 64, 128$, and 256 for $p = 1, 3$, and 7; The corresponding effective horizontal grid spacing at the equator is $\Delta_{h,\mathrm{eq}} = 313, 156, 78$ and 39 km. For $p = 11$, we changed it as $N_{e,h}(p+1) = 24, 48, 96$, and 192, which correspond to $\Delta_{h,\mathrm{eq}} = 417, 208, 104$, and 52 km. As a temporal scheme, we adopted a fully explicit fourth-order RK scheme described in Sect. 2.4.2. The Courant number for advection $u_0 \Delta t / \Delta_{h,\mathrm{eq}}$ was set to be about 0.6. In this experiment, modal filter was not used because the upwind numerical flux provided a sufficient numerical stabilization.

Figure 1 shows the numerical errors after one period ($t = 12$ days). As theoretically expected, we obtain about $p+1$-order spatial accuracy for L_1, L_2, and L_{inf} errors. For $p = 11$ in the high spatial resolutions, the discretization error with the fourth-order temporal scheme, or the round-off error, degrades the convergence rate of 12th-order spatial accuracy. In the figure, the dashed lines represent the error norms in the case of $\alpha = \pi/4$ radian when the Gaussian profile passes over the singular points on cubed-sphere mesh. Their magnitudes are similar to that obtained for $\alpha = 0, \pi/2$ radians, which are represented by solid and dashed lines. Even for $p = 1$, there is less difference between the angles of rotation axis. Thus, when applying DGM to the advection problem, we consider the influence of singularity with the cubed-sphere coordinate to be quite small.

3.2 Internal gravity wave

To check wave propagation with pressure gradient and buoyancy terms, test cases of gravity wave are often utilized; For example, Tomita and Satoh (2004) also performed an internal gravity wave test. However, the basic state and initial perturbation

https://doi.org/10.5194/egusphere-2024-1477
Preprint. Discussion started: 12 June 2024

produce vertically high modes and nonlinear terms can develop small structures. This is inconvenient for investigating numerical convergence. On the other hand, the experimental setting based on Baldauf and Brdar (2013), which originally assumed a two-dimensional computational domain, can focus on a single mode. This study considered a global domain version of gravity wave test in Baldauf and Brdar (2013). The initial condition is a rest isothermal atmosphere of $T_0 = 300$ K, which corresponds to a constant Brunt Väisälä frequency of $\sqrt{g^2/(C_pT_0)} \sim 1.8 \times 10^{-2}$ s^{-1}. Further, we added a small temperature perturbation with a Gaussian profile as

$$T' = \Delta T \exp\left(-\frac{d}{D}\right) \sin\left(n_v \pi \frac{z}{z_T}\right) \exp\left(-\frac{g}{2RT_0} z\right),$$

where ΔT is the amplitude, D is the characteristic horizontal scale, n_v is the index with vertical mode, and d is calculated from Eq. (19). In this experiment, we set to $z_T = 10$ km, $\Delta T = 0.01$ K, $D = a/5$, $n_v = 1$, and $(\lambda_c, \theta_c) = (0, \pi)$, The Coriolis force and topography were not considered.

The horizontal and vertical effective grid spacing were changed as (313 km, 417 m), (156 km, 208 m), (78 km, 104 m), and (39 km, 52 m) using $p = 1, 3$, and 7. Whereas, for $p = 11$, they were changed as (208 km, 417 m), (104 km, 208 m), and (102 km, 104 m). As the temporal scheme, we adopted an IMEX Runge–Kutta scheme with the third-order accuracy, as described in Sect. 2.4.1. For the HEVI scheme, we set the Courant number against the horizontally propagating sound wave as $C_{rh,cs} \sim 0.134$ for $p = 1, 3, 7$ and $C_{rh,cs} \sim 0.126$ for $p = 11$. To investigate the impact of temporal error, we also conducted additional experiments with smaller timesteps for $p = 7$ and $p = 11$ where the above Courant number value was reduced by factors of $1/2$ and $1/4$. In the absence of modal filter, the self-convergence of numerical solutions were investigated. The reference solution was obtained from a high-resolution experiment where horizontal and vertical grid spacing were (20 km, 26 m) with $p = 7$ and $C_{rh,cs} \sim 0.067$.

To present the temporal evolution of gravity wave, Figure 2 shows the spatial distribution of potential temperature, and zonal and vertical winds after $t = 0.5$ days and $t = 2$ days. Based on this result, the horizontal phase speed is estimated to be about 58 m s^{-1}. This result corresponds well to the linear theoretical value under the hydrostatic approximation, $Nz_T/(\pi n_v) \sim 57$ m s^{-1}.

Figure 3 shows the dependence of error norms on spatial resolutions for the density perturbation (ρ'), horizontal wind (u^ξ), vertical wind(w), and perturbation of potential temperature weighted density ($(\rho\theta)'$). For relatively low-order p such as $p = 1$ and $p = 3$, almost $p+1$-order accuracy is observed for the four variables in sufficiently high spatial resolutions. However, due to the fast wave modes, temporal errors for the third-order HEVI scheme can dominate over the spatial errors in the cases of large p and high-resolution. This behavior is evident for the error norms of all variables except the horizontal wind. For the case of $p = 7$ with $C_{rh,cs} \sim 0.134$, the numerical convergence rate has about third-order slope for ρ' and $(\rho\theta)'$, and it has between second- and third-order slope for w. As the time step decreases, the numerical convergence rate for $p = 7$ approaches almost $p+1$-order. Even for the case of small Courant number, due to increase in round-off errors, the reduction in the error norms for ρ' and u^ξ stops as the spatial resolution increased. For $p = 11$, this problem of round-off errors is worse; Stagnating error reduction appears in the spatial resolutions lower than that in $p = 7$ and the errors increased with the spatial resolution. Note that the influence of round-off error might be overestimated because the amplitude of initial perturbation was significantly

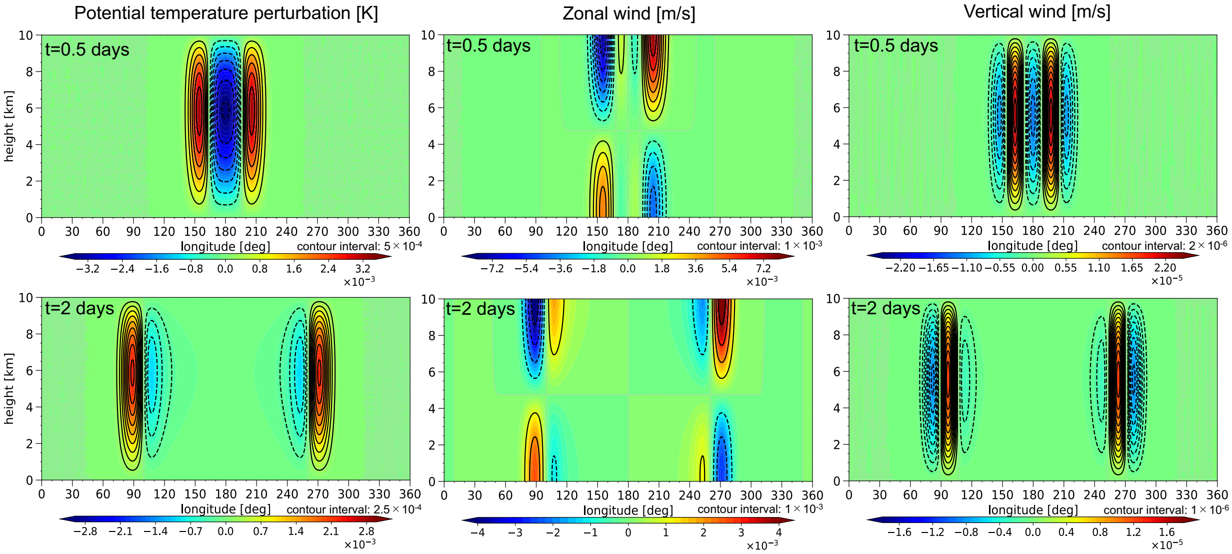

Figure 2. The spatial distribution of potential temperature, and zonal and vertical wind at the equator after $t = 0.5$ days (upper panel) and $t = 2$ days (lower panel) obtained from a gravity wave test case with $(\Delta_{h,\mathrm{eq}}, \Delta_v)$ =(78 km, 104 m) using $p = 7$.

small and no modal filter was used in this experiment. Thus, the problem is considered to be not critical in practical simulations including the modal filtering or turbulent schemes.

3.3 Mountain wave

Adopting the basic terrain-following coordinate introduced in Sect. 2.1 together with low-order schemes is well known to produce large numerical errors with pressure gradient terms and to develop spurious flows. However, such issues can be avoided using high-order DGM. To check the numerical behavior of the basic terrain-following coordinate in high-order DGM, we performed a mountain wave test on a reduced planet radius based on Klemp et al. (2015) (referred to as KSP2015) and the test case 2-1 in Dynamical core model intercomparison project (DCMIP) test case document (Ullrich et al., 2012). Here, the planetary radius was set to a/X_r, where $X_r = 166.7$ is the scaling factor. In this experiment, the rotation was not considered. KSP2015 considered a topography profile in the form of

$$h^{\mathrm{KSP2015}}(\lambda,\theta) = h_0 \exp\left(-\frac{\tilde{d}^2}{d_0^2}\right)\cos^2\left(\pi\frac{\tilde{d}}{d_1}\right)\cos\theta,$$

where $\tilde{d} = a/X_r(\lambda - \lambda_c)$ (here, $\lambda_c = \pi$), $d_0 = 5000$ m, and $d_1 = 4000$ m. The maximum height of mountain h_0 was set to 25 m. In the topography profile, the mountain wave structure along the equator is comparable to the results with two-dimensional Schär type mountain (Schär et al., 2002). On the other hand, from the perspective of investigating the numerical convergence, it is undesirable for the zonal scale of topography to decrease with the latitudes and eventually become zero at the poles. To ensure that the minimum horizontal scale is sufficiently resolved in high resolution simulations, the undulation of the mountain

https://doi.org/10.5194/egusphere-2024-1477
Preprint. Discussion started: 12 June 2024

(a) Density (ρ')

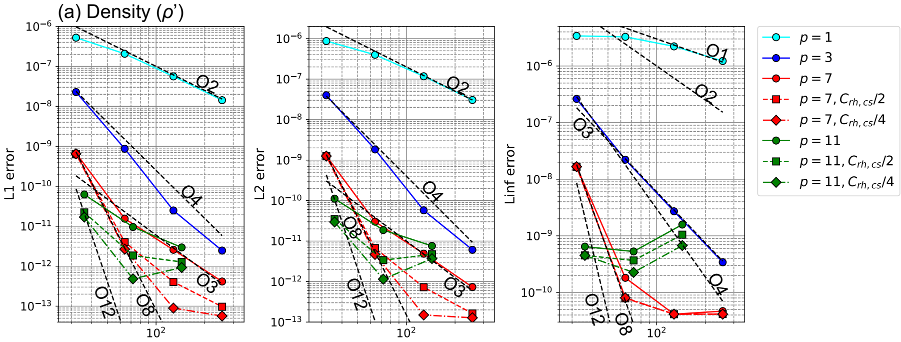

(b) Horizontal wind (u^{ξ})

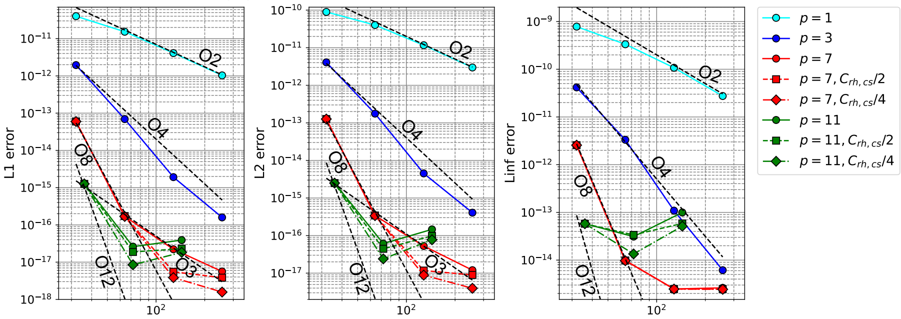

(c) Vertical wind (w)

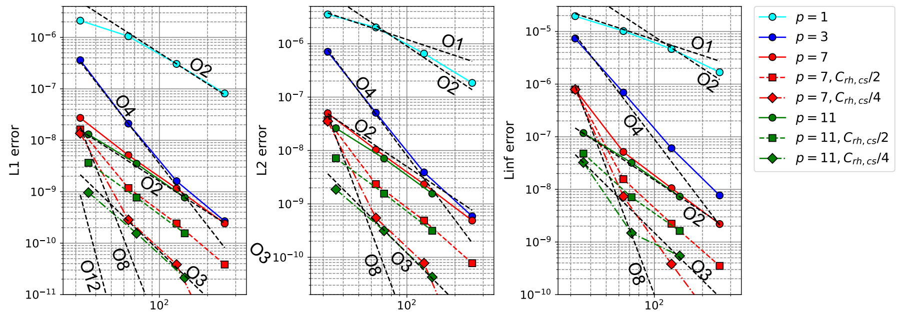

(d) Density x Potential temperature (($\rho\theta$)')

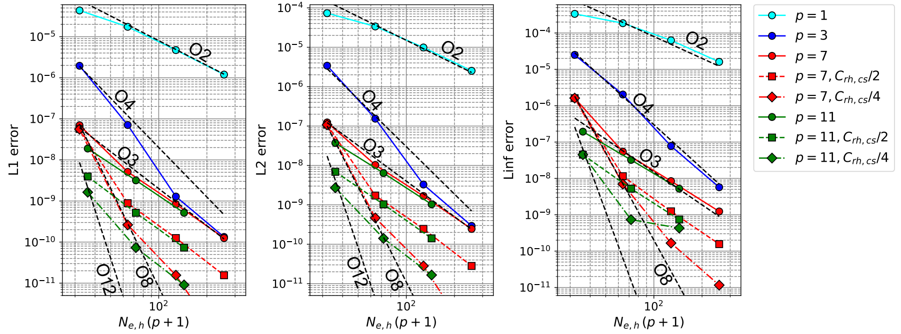

Figure 3. Dependence of L_1, L_2, and L_{inf} errors on spatial resolution for (a) density perturbation (ρ'), (b) horizontal wind (u^{ξ}), (c) vertical wind (w), and (d) perturbation of potential temperature weighted density ($(\rho\theta)'$) after $t = 2$ days in a gravity wave test case.

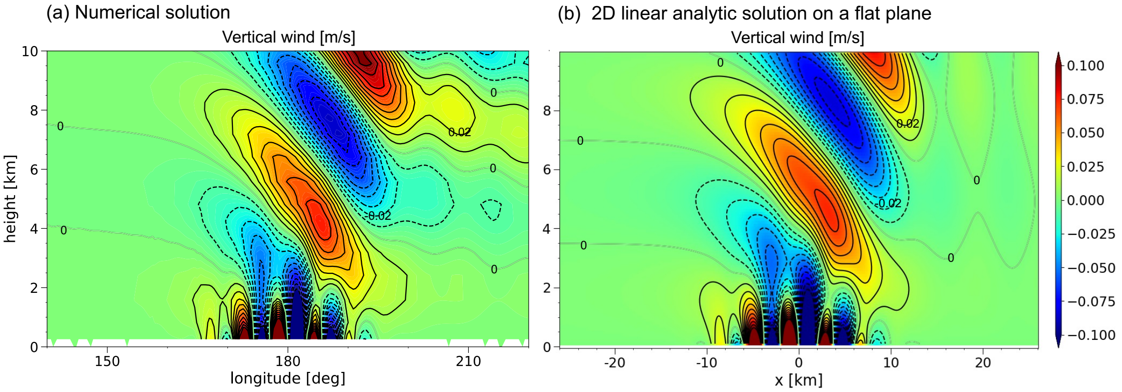

Figure 4. The spatial distribution of vertical wind at the equator obtained from a mountain wave test case with a Schär-like mountain: (a) Numerical solution at $t = 2$ hours obtained from $(\Delta_{h,\text{eq}}, \Delta_v)$ =(625 m, 500 m) using $p = 7$, (b) Two-dimensional linear analytic solution on a flat plane (shown for comparison).

is eliminated at the high latitudes using a tapering function as

$$h(\lambda,\theta) = h^{\text{KSP2015}}(\lambda,\theta)\,\frac{1}{2}\left[1+\tanh\left(\frac{|\theta|-\pi/3}{8\pi/180}\right)\right]. \tag{20}$$

As initial condition, we assumed a rest isothermal atmosphere of 300 K. KSP2015 considered an impulsive start where a zonal wind in solid body rotation ($u = U_0 \cos\theta$ where $u_0 = 20$ m s^{-1}) and the corresponding balanced state were initially given. However, such impulsive start produces initial shocks with small spatial scales, which complicates the discussion on the numerical convergence. To mitigate the influence of impulsive start, we gradually accelerated the wind using relaxation terms with the time scale of 60 s. For further details, refer to Appendix A1.

The horizontal and vertical effective grid spacing (at about $z < 15$ km) changed as (625 m, 500 m), (313 m, 250 m), and (156 m, 125 m) using $p = 3, 7$, and 11. The model top was set to 30 km. As the temporal scheme, a fully explicit fourth-order RK scheme was used. The Courant number against the propagating sound wave was fixed to $C_{\text{rh,cs}} \sim 0.263$. The reflection of waves at the model top was suppressed by introducing a sponge layer and gradually increasing the vertical grid spacing at about $z > 15$ km. Moreover, a lateral sponge layer was placed on the 1/4 sector of the sphere to reduce the disruption of targeting mountain wave structure by initial shocks globally propagating. For the details of sponge layer, refer to Appendix A2. The reference solution was obtained from a high-resolution experiment where the horizontal and vertical grid spacing were (78 m, 62.5 m) with $p = 7$. In this test case, to ensure the numerical stability, we used a weak modal filter, which are summarized in Table. 5.

Figure 4(a) shows the spatial distribution of vertical wind after 2 hours. For a comparison, a linear analytic solution on a flat plane in the two-dimensional Cartesian coordinates is shown in Fig. 4(b) (The derivation can be found in Appendix A of KSP2015, for example). Since the characteristic wavelength of mountain scaled by the Scorer parameter is $d_0 N/U_0 \sim$ O(1), this setting corresponds to a nonhydrostatic regime of mountain wave. In such regime, the waves with small-scale wavelengths are trapped near the surface, while large-scale waves propagate upward. The obtained wind pattern well reproduces that shown

https://doi.org/10.5194/egusphere-2024-1477
Preprint. Discussion started: 12 June 2024

in Fig. 2(a) of KSP2015. On the other hand, the numerical solution and the linear analytic solution on a flat plane is slightly different. We consider that the difference decreases as the planetary radius increases in addition to optimizing the sponge layer.

Figure 5 shows the dependence of error norms on spatial resolutions for the density perturbation (ρ'), horizontal wind (u^{ξ}), vertical wind (w), and perturbation of potential temperature weighted density ($(\rho\theta)'$). A comparison performed at the fixed DOF shows that the numerical errors decrease with the increase in polynomial order, although the numerical convergence rate is smaller than $p+1$-order accuracy. For example, the slope of L_2 error norm is about 3/4 of that with $p+1$-order accuracy. Based on additional experiments with the corresponding two-dimensional setup, the sub-optimal convergence can be related to several factors such as the modal filter and the spatial discretization for Jacobian cofactors ($\sqrt{G_v}G_v^{13}$ and $\sqrt{G_v}G_v^{23}$). For further details, refer to Appendix A3.

3.4 Baroclinic instability

Baroclinic instability is a typical phenomenon in mid-latitude. It includes small-scale structures such as front and filament formations are included. We conducted an idealized numerical experiment based on Jablonowski and Williamson (2006) (referred to as JW2006). In the aspect of numerical method, dynamical cores must accurately represent the wave growth process. In addition, it is necessary to treat the developing small-scale flow structures while ensuring numerical stability. As for the experimental setup, the initial zonally symmetric fields can be expressed using the analytic expressions of a steady-state solution of adiabatic inviscid primitive equation. To trigger baroclinic instability, a perturbation of zonal wind with a Gaussian profile is added in the Northern hemisphere. For further details on parameter values, refer to Sect. 2(a) of JW2006.

We investigated on the dependence of numerical solutions on the horizontal resolution as performed in JW2006. The horizontal effective grid spacing $\Delta_{h,\mathrm{eq}}$ changed as 250 km, 125 km, 63 km, and 32 km with a fixed total vertical DOF of 24 for $p = 3$ and 7, whereas it changed as 208 km, 104 km, and 52 km with a fixed total vertical DOF of 36 for $p = 11$. We used a stretch vertical grid spacing such that the effective vertical grid spacing Δ_v near the surface became about 350 m. For the third-order HEVI scheme, we set the Courant number against the horizontally propagating sound wave as $C_{rh,cs} \sim 0.14$. Furthermore, the modal filter was utilized to maintain the numerical stability. Its parameters are summarized in Table 6. When calculating the L_2 error of surface pressure, we used the results obtained from the corresponding highest resolution experiment for each p as the reference solution. If the vertical spatial errors have similar values among different horizontal resolution cases, the vertical errors virtually cancel out. Thus, we can directly discuss the behavior of numerical convergence associated with the horizontal spatial or temporal accuracy.

Figure 6 shows the temporal evolution of baroclinic wave for the case of $\Delta_{h,\mathrm{eq}} = 63$ km using $p = 7$. The obtained horizontal distributions of surface pressure and temperature at 850 hPa are similar to those reported in the previous studies. For example, see Fig. 5 in JW06, which is obtained from the FV dynamical core (Lin and Rood, 1996, 1997). The wave grows very slow for 4 days. After that, the highs and lows deepen significantly and the wave begins to break at the 8-th day. Figure 7 shows dependence of the surface pressure and temperature at 850 hPa (after 9 days) on the horizontal spatial resolution for $p = 7$. The same figure obtained from the FV dynamical core can be seen in Fig. 6 of JW06. Our dynamical core provides reasonably accurate numerical solutions at high spatial resolution experiments. These solutions are comparable to the reference solutions

https://doi.org/10.5194/egusphere-2024-1477
Preprint. Discussion started: 12 June 2024

(a) Density (ρ')

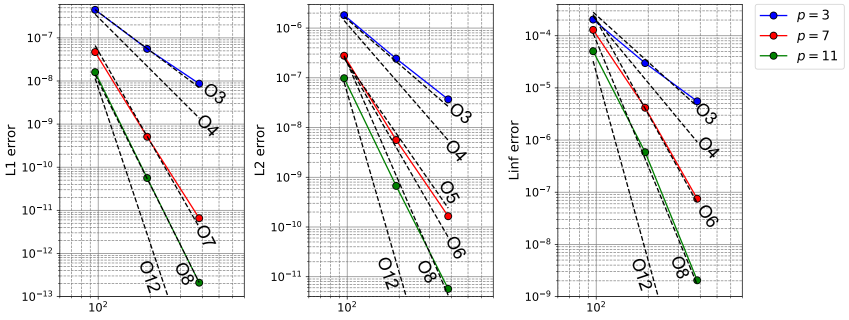

(b) Horizontal wind (u^ξ)

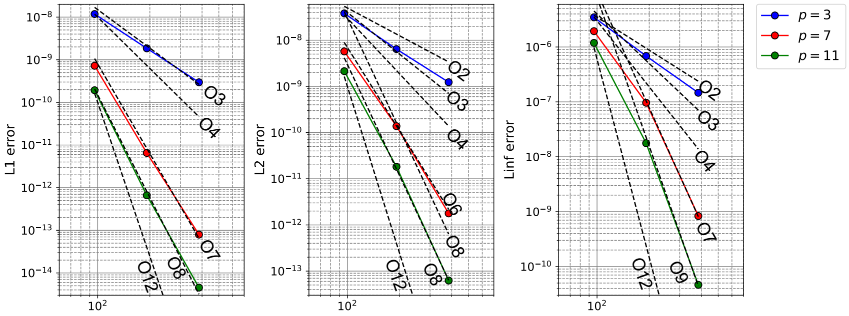

(c) Vertical wind (w)

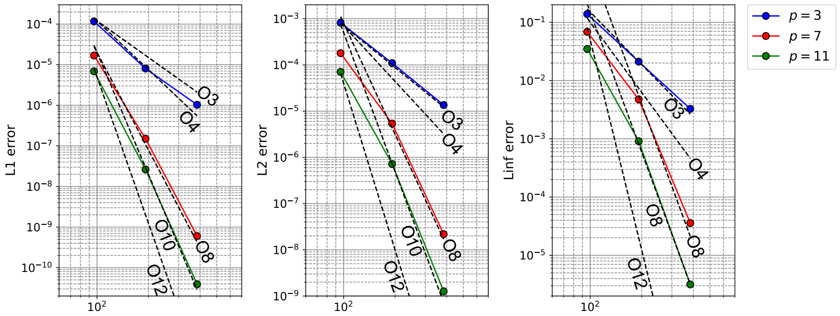

(d) Density x Potential temperature ((ρθ)')

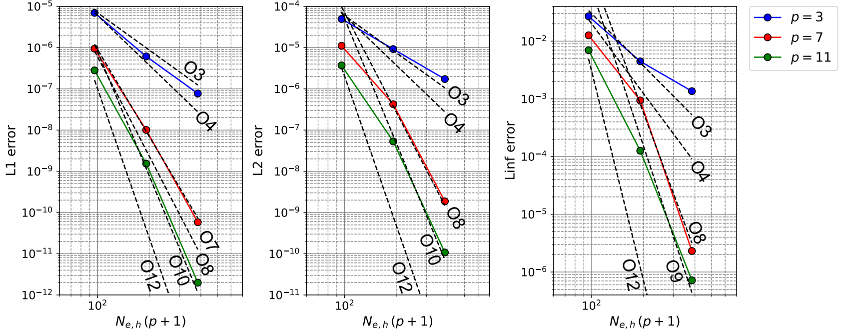

Figure 5. Dependence of L_1, L_2, and L_{inf} errors on spatial resolution for (a) perturbation of density (ρ'), (b) horizontal wind (u^ξ), (c) vertical wind (w), and (d) perturbation of potential temperature weighted density ($(\rho\theta)'$) after 2 hours in a mountain wave test case.

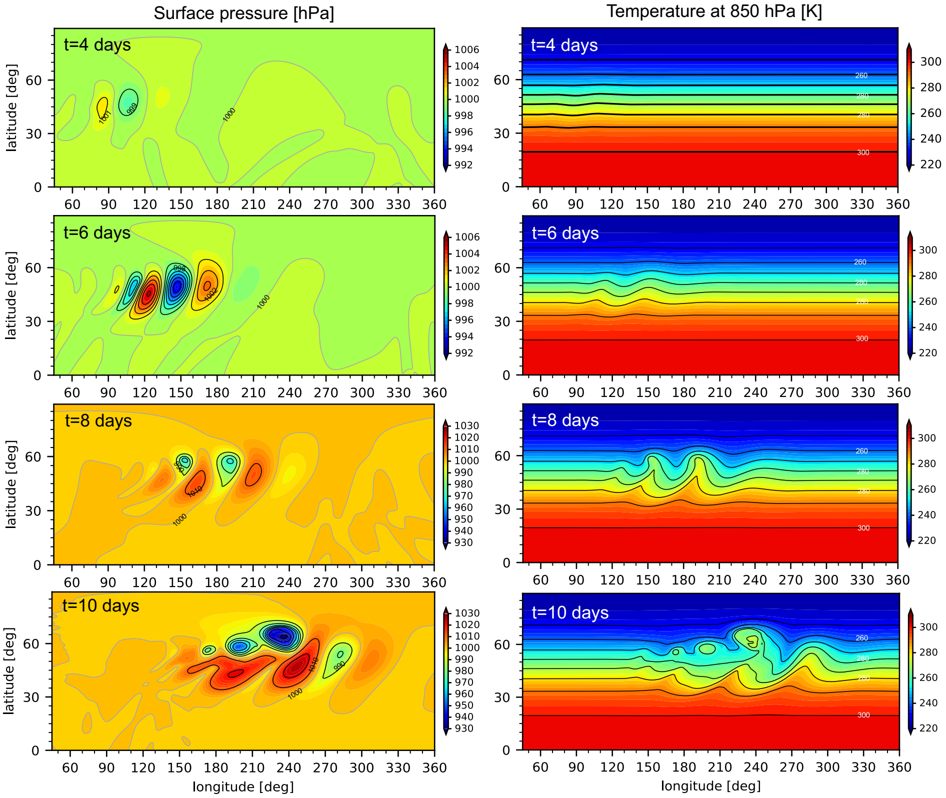

Figure 6. Spatial distribution of the surface pressure and temperature at 850 hPa after $t = 4, 6, 8$, and 10 days in a baroclinic instability test. We present the results obtained from the experiment using $p = 7$ with $\Delta_{h,\mathrm{eq}} = 63$ km and vertical DOF of 24.

reported in the previous studies. In addition, the effective resolution is apparently higher than that of the low-order global dynamical core. For example, in the marginally resolved simulation setting, $\Delta_{h,\mathrm{eq}} \sim 250$ km, the amplitude and phase errors are small.

For a quantitative evaluation for horizontal resolution dependence, Figure 8 shows the temporal evolution of L_2 error norm of the surface pressure for $p = 3, 7$, and 11. In the figure, the gray shade represents the uncertainty range of reference solutions estimated by various dynamical cores in JW2006. In our evaluation strategy, due to the cancelation of vertical errors between different horizontal resolutions for each p, we successfully captured the numerical convergence with horizontal discretization and temporal errors. The L_2 errors until about 6 days (except initial adjustment stage) decreases with horizontal resolution. The magnitude is significantly small compared to that in previous studies (for example, the FV dynamical core and Mcore (Ullrich and Jablonowski, 2012b)). After 6 days when the baroclinic wave starts to develop significantly, the L_2 errors rapidly grow and the difference between horizontal resolutions decreases. For $p = 3$, the feature of numerical convergence at the mature stage is similar to that obtained from MCore. In summary, the L_2 errors for $\Delta_{h,\mathrm{eq}} < 250$ km are within the uncertainty range suggested by JW2006. Thus, we consider that the numerical solutions obtained from the proposed model are reasonable.

https://doi.org/10.5194/egusphere-2024-1477
Preprint. Discussion started: 12 June 2024

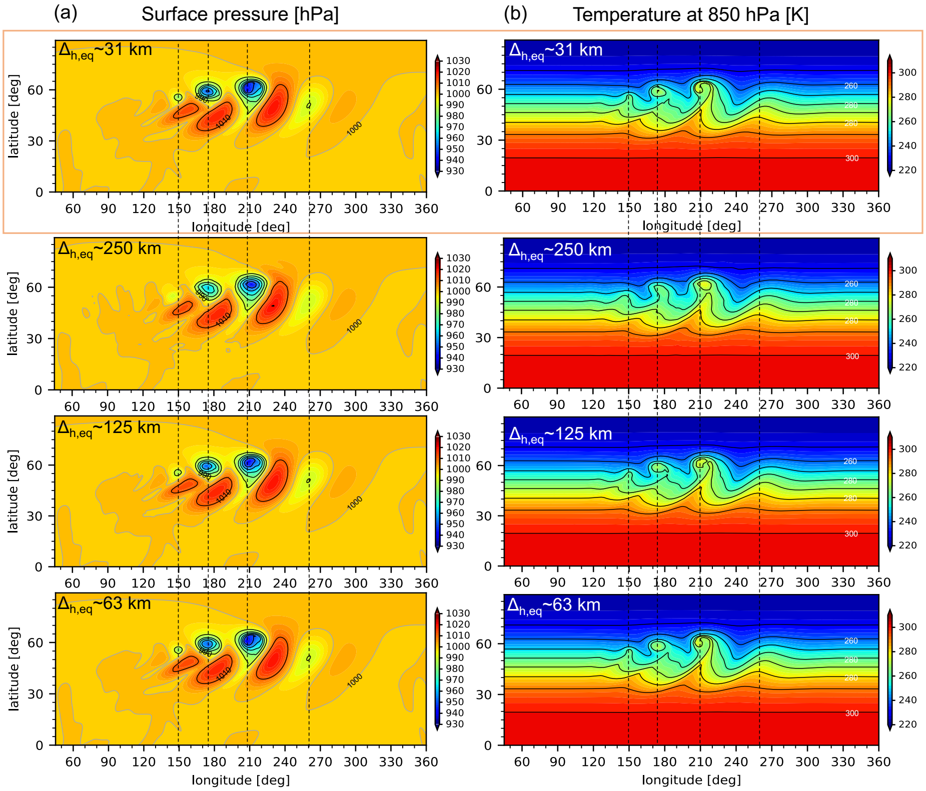

Figure 7. Horizontal resolution dependence of (a) surface pressure and (b) temperature at 850 hPa after $t = 9$ days in a baroclinic instability test. We present the results obtained from the experiments using $p = 7$ with the vertical DOF of 24.

3.5 Held–Suarez test

As a long-term idealized benchmark toward real climate simulations, we conducted the Held–Suarez test (Held and Suarez, 1994), which uses a prescribed forcing that mimics complex physics parameterization. The boundary-layer friction is represented in a form of Rayleigh damping. The diabatic heating/cooling effect is represented using a Newtonian relaxation term to a prescribed temperature in radiative equilibrium T_e. For further details on these terms, see p.1826 in Held and Suarez (1994). In this study, a rest atmospheric field in hydrostatic balance with T_e was given as the initial condition.

To investigate the spatial resolution dependence, the effective grid spacing $\Delta_{h,\mathrm{eq}}$ and vertical DOF changed as (208 km, 32), (104 km, 64), and (52 km, 128) for $p = 3, 7$, and as (208 km, 36), (104 km, 72), and (52 km, 144) for $p = 11$. The vertical grid spacing was stretched. For example, when the vertical DOF is 32, the effective vertical grid spacing near the surface becomes about 350 m. For the cases of $\Delta_{h,\mathrm{eq}} = 208, 104$, and 52 km, the temporal integration was performed for at least 1200 days; The first 200-days data was discarded during the statistical analysis. For high resolution cases of $\Delta_{h,\mathrm{eq}} = 52$ km and 26 km, the results after the spin-up period with coarser resolutions were used as the initial data, and shorter temporal integration was conducted because of the limited computational resources. As the temporal scheme, we adopted the third-order HEVI scheme

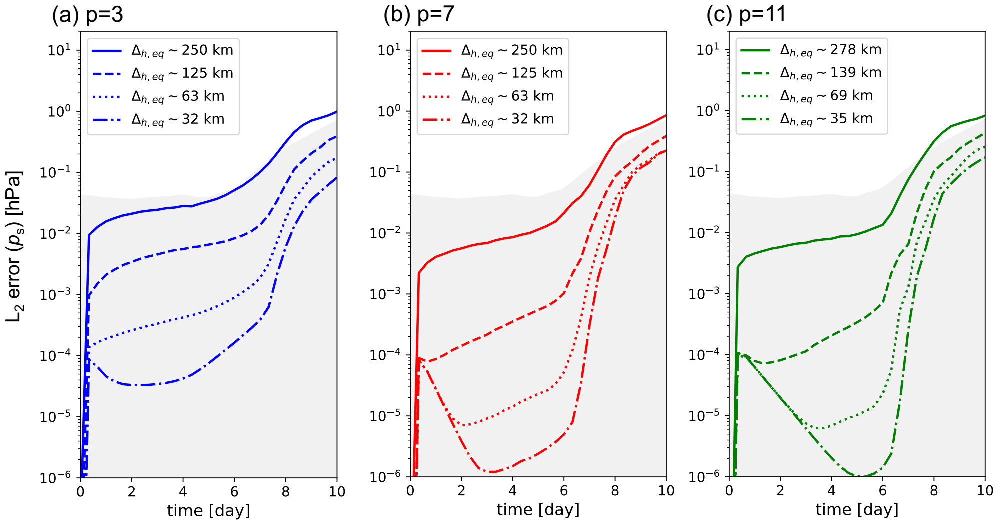

Figure 8. Dependence of the L_2 error norm for surface pressure on horizontal spatial resolution in a baroclinic instability test using (a) $p = 3$, (b) $p = 7$, (c) $p = 11$. Note that the reference solution for each p is the result from the corresponding highest resolution experiment.

with the Courant number against the horizontally propagating sound wave of $C_{rh,cs} \sim 0.13$. Moreover, we used the modal filters summarized in Table 7. To stabilize long temporal integrations with nonlinear flow processes, note that the large decay coefficients were set. The reference solution was obtained from a high-resolution experiment where $\Delta_{h,\text{eq}}$ and vertical DOF were (26 km, 256) with $p = 7$.

Figure 9 shows the atmospheric fields in a statistical equilibrium state for $\Delta_{h,\text{eq}} = 208$ km using $p = 7$. The obtained pattern and strength of general circulations are similar with the results obtained by using nearly spatial resolution in previous studies (e.g., Wan et al., 2008). For a single westerly jet in each hemisphere, a maximum velocity of about 30 m s^{-1} is obtained at $p = 250$ hPa. Easterlies exist in equatorial and polar lower atmosphere and near the model top at low latitude. As shown in Fig. 9(c)-(f), the baroclinic wave activity in the proposed DG model is similar to that reported in previous studies. At $p = 250$ hPa in the mid-latitudes, the magnitude of eddy momentum flux reaches about 70 m^2/s^2. The maximum of poleward eddy heat flux is located at $p = 850$ hPa in the midlatitude; its values reaches about 22 K m s^{-1}. The eddy kinetic energy and temperature variance reach maximum values of about 430 m^2/s^2 at $p = 250$ hPa and 45 K^2 at $p = 800$ hPa in the midlatitude, respectively.

As discussed in a previous study (Wan et al., 2008), these eddy quantities such as the eddy kinetic energy and temperature variance are sensitive to the spatial resolutions. As shown in Figs. 10(a), (c), the absolute peak values increase with the spatial resolutions and begin to converge when the horizontal grid spacing is less than about 50 km. The convergence of peak values with $p = 7, 11$ is faster than that in the case of $p = 3$. For comparison, the corresponding peak values indicated from previous studies are shown by the colored boxes in the figure. The obtained trend of spatial resolution dependence for $p = 3$ is similar to that reported by studies by conventional low-order grid point methods (Tomita and Satoh, 2004; Wan et al., 2013). On the

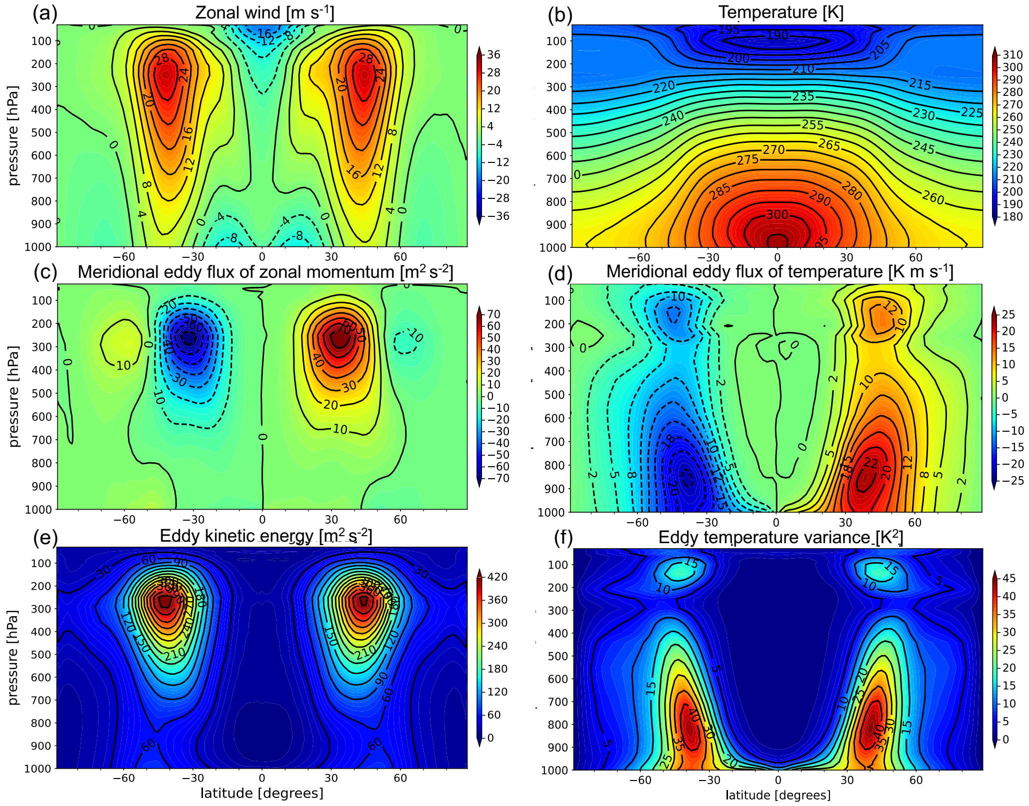

Figure 9. Zonally and temporally averaging atmospheric fields in a statistical equilibrium state: (a) zonal wind, (b) temperature, (c) meridional eddy flux of zonal momentum, (d) meridional eddy flux of temperature, (e) eddy kinetic energy, and (f) eddy temperature variance obtained from a Held–Suarez test with $\Delta_{h,\mathrm{eq}} = 208$ km using $p = 7$. As is typically done in previous studies, when taking the zonal and temporal average, we used the 1000-days data after the spin-up calculation.

other hand, the peak values from $p = 7, 11$ at the horizontal grid spacing of about 200 km are similar to the results obtained by using the horizontal spectral method (Wan et al., 2008).

Figure 11 shows kinetic energy spectra of horizontal winds at $p = 850$ hPa and $p = 250$ hPa. As reported in previous studies (e.g., Malardel and Wedi, 2016; Tolstykh et al., 2017), the obtained spectra have the n^{-3} slope at the spherical harmonic degrees between 10 ∼ 100. The steep slope compared to −3 reflects the influence of numerical dissipation mechanism with upwind numerical flux and modal filter. For the cases of $p = 7, 11$, the obtained energy spectra well follow that for the reference experiment at the wavelengths longer than about eight grids. In the spatial resolution dependence of peak values with the eddy quantities shown in Fig .10, there is no significant difference between $p = 7$ and $p = 11$, whereas the improvement of effective resolution by higher polynomial order of $p = 11$ can be observed in the energy spectra as the grid spacing decreases. For $p = 3$, the energy spectra overlap with that of the reference experiment up to about 10∼20 grids. Furthermore, for $\Delta_{h,\mathrm{eq}} = 208$ km with $p = 3$, the spectra are entirely smaller than the reference solution. Thus, using strong modal filters to ensure numerical stability

https://doi.org/10.5194/egusphere-2024-1477
Preprint. Discussion started: 12 June 2024

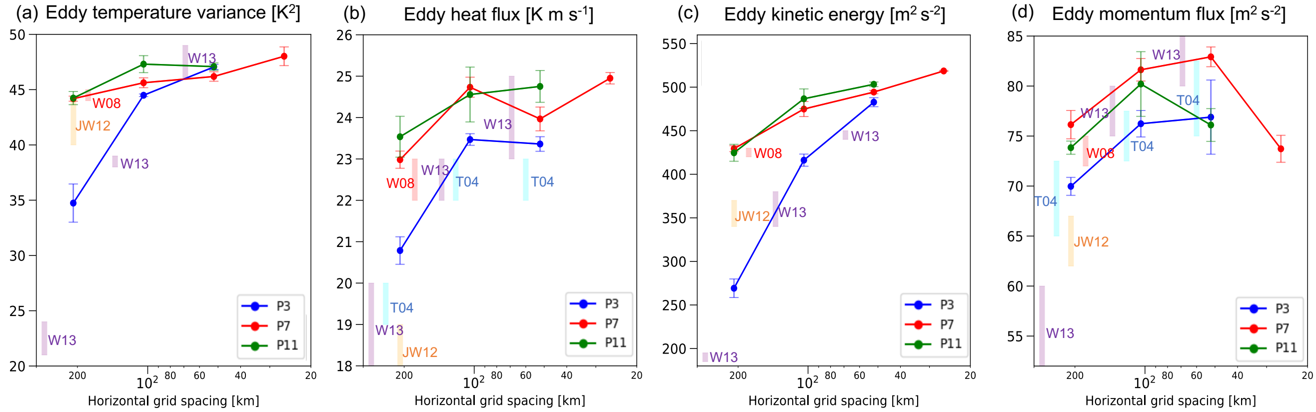

Figure 10. Dependence of absolute peak values on the spatial resolution: (a) eddy temperature variance, (b) eddy heat flux, (c) eddy kinetic energy, (d) eddy momentum flux. The time averaging period is the same as that in Fig. 10. In each panel, the difference between the Northern and Southern hemispheres is represented using the error bars. The colored boxes labeled by T04, W08, UJ12, and W13 denote the corresponding peak values indicated by the results reported in Tomita and Satoh (2004), Wan et al. (2008), Ullrich et al. (2012), and Wan et al. (2013), respectively; Because the peak values were estimated from the contour figures, note that the uncertainty is large, and its range is roughly represented by the box height.

for long-term integration has a significant effect on the spectra and effective resolutions in relatively small polynomial order. These results indicate that there is room for improving our treatment of the nonlinear terms to weaken the modal filters.

3.6 Planetary boundary layer turbulence experiment on a small planet

As a first step toward future global LES with O(10 m) grid spacing, we performed a global extension of the LES experiment of idealized planetary boundary layer turbulence in Nishizawa et al. (2015), KT2021, and KT2023. Currently, it is not feasible to conduct a global LES for a planetary size of Earth using a uniform spatial resolution of O(10 m). To save the required computational resources, the planetary radius set to be 3.4 km here. Although this value is significantly different from that in realistic planets such as Earth and the effect of spherical geometry may affect the convection structure, we consider that this test is useful to validate the turbulent model described in Sect. 2.2. We focused on the case of applying the shallow atmosphere approximation because we expected the results to be comparable to the results reported in our previous studies. This approximation is obviously unsuitable for discussing physical aspect in this experimental setting; For the case without approximation, refer to Appendix B. The experimental setup is as follows: The altitude of model top was set to 3 km. There were no rotation and topography. Initially, we set a stable stratification with a vertical gradient of potential temperature of 4 K/km and added random perturbations with an amplitude of 1 K. Since it is difficult to consider a uniform wind in the global situation, there is no initial motion in contrast to that in our previous studies. To drive thermal convections, a constant heat flux with 200 W m^{-2} was imposed at the surface. To focus on the validation of turbulent model, radiation and moist processes were

https://doi.org/10.5194/egusphere-2024-1477
Preprint. Discussion started: 12 June 2024

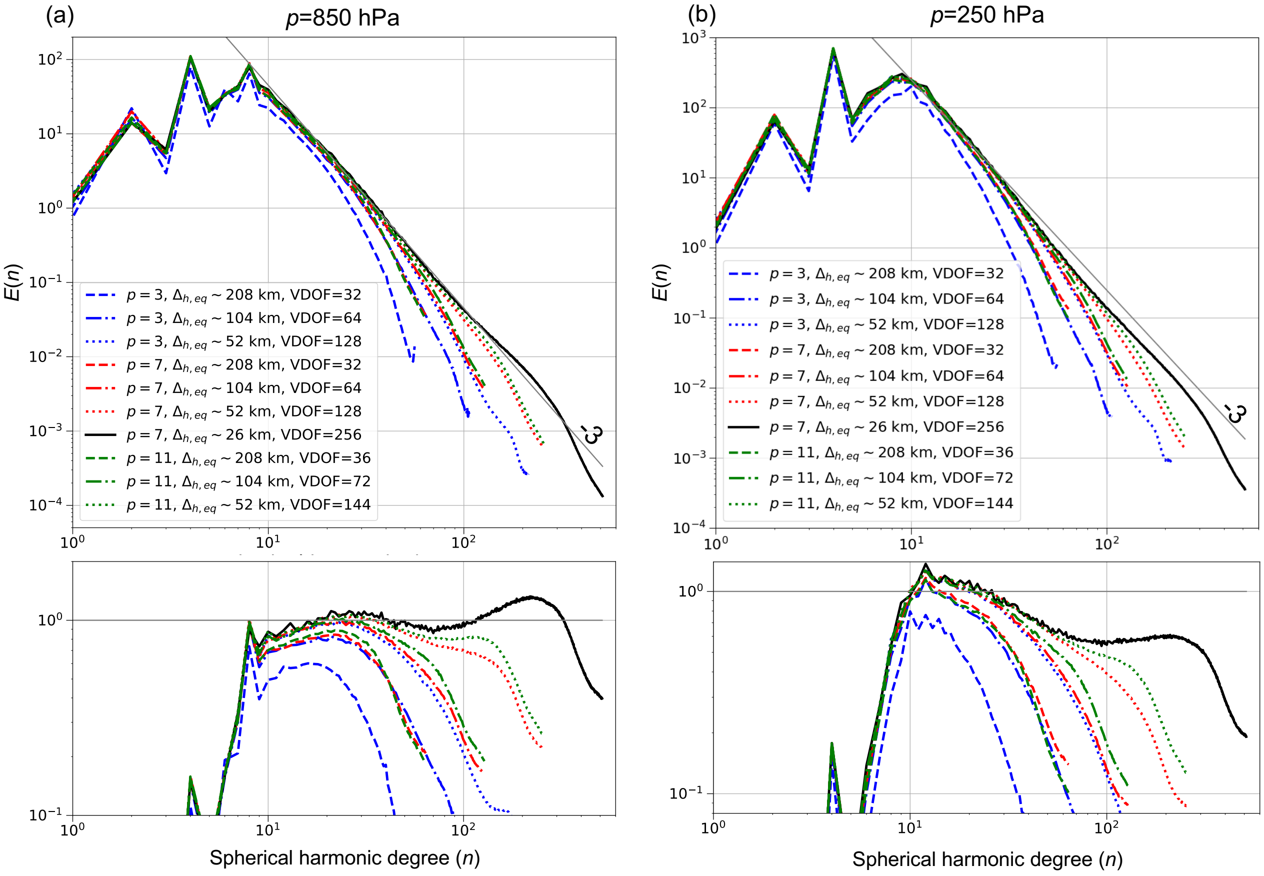

Figure 11. Energy spectra of horizontal wind in a statistical equilibrium state at (a) p = 850 hPa and (b) p = 250 hPa in a Held–Suarez test. As explained in the legend, the difference between spatial resolutions is represented by line types, and the line color indicates the polynomial order. The results from the reference experiment are shown by solid black lines. Lower panels represent the compensated spectra, which is proportion to $E(n)n^3$. The temporal average was calculated over 1000 days after the spin-up period; In the highest resolution case ($\Delta_{h,\mathrm{eq}} = 26$ km), it was performed over 300 days.

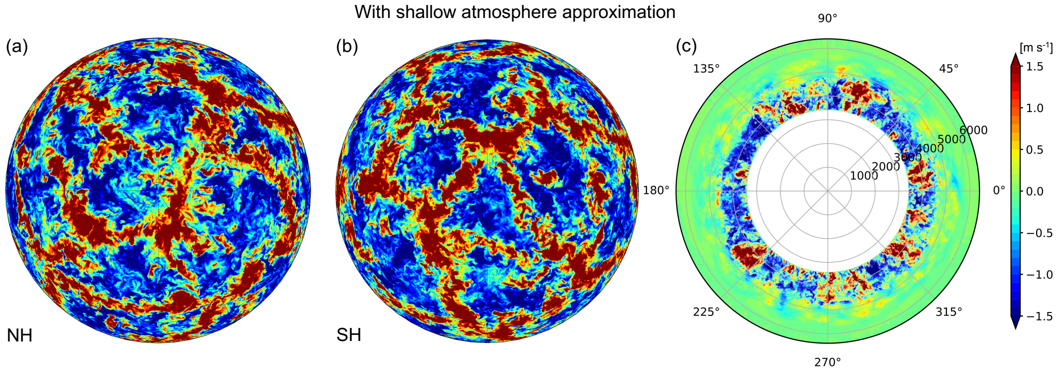

Figure 12. The horizontal distribution of vertical wind at $z = 500$ m after $t = 4$ hours when the shallow atmosphere approximation is applied: (a) Northern hemisphere (NH), (b) Southern hemisphere (SH), and (c) their corresponding cross-sections along the equator.

not considered. In the turbulent model, we set the filter length to double that of effective local grid spacing, which is same as that in our previous studies. A reflection of waves at the model top is prevented using a sponge layer located above $z = 2$ km.

To check the impact of polynomial order on the energy spectra in the same context as KT2023, we changed p as $3, 4, 7$ while setting the effective grid spacing to be about 10 m. Numerical stability was ensured by using a modal filter with parameters $p_{m,h} = p_{m,v} = 32$ and $\alpha_{m,h} = \alpha_{m,v} = 10^{-3}$. As the temporal scheme, a fully explicit fourth-order RK scheme described in Sect. 2.4.2 was used for the inviscid terms, whereas the forward Euler scheme was adopted for the SGS terms. The time step was set to 0.0125 s; The corresponding Courant number for the sound wave is about 0.438. The integration time was 4 hours for the case of $p = 7$. To reduce the computational cost, the output at 3 hours was used as the initial condition of the other experiments for which the integration time was 1 hour.

Figure 12 shows the horizontal distribution for vertical wind at $z = 500$ m and cross-section along the equator after $t = 4$ hours in the case of $p = 7$. The convective cells have polygonal structures with a horizontal scale of about 2-3 km. The height of PBL reaches between 1–1.5 km. To present the vertical structure of PBL, Figure 13 shows the vertical distribution of potential temperature, turbulent transport of heat and momentum, and skewness of vertical wind for $p = 7$. In these panels, the gray shade represents the results obtained from KT2023 using the plane regional model. The results obtained in this study are well similar to those reported in KT2023.

Figure 14 shows the kinetic energy spectra of three-dimensional wind at $z = 500$ m, which was temporally averaged during the last 30 minutes. The features of the obtained energy spectra are similar to those reported in KT2023. At longer wavelengths than eight grids, the slope of spectra was about $-5/3$. On the other hand, the slope of spectra at the shorter wavelength range deepens due to the turbulent model, numerical dissipation with the upwind numerical flux, and modal filter used in this study. KT2023 indicated that the required polynomial order is $p > 3$, which is true for global LES based on the results obtained in this study.

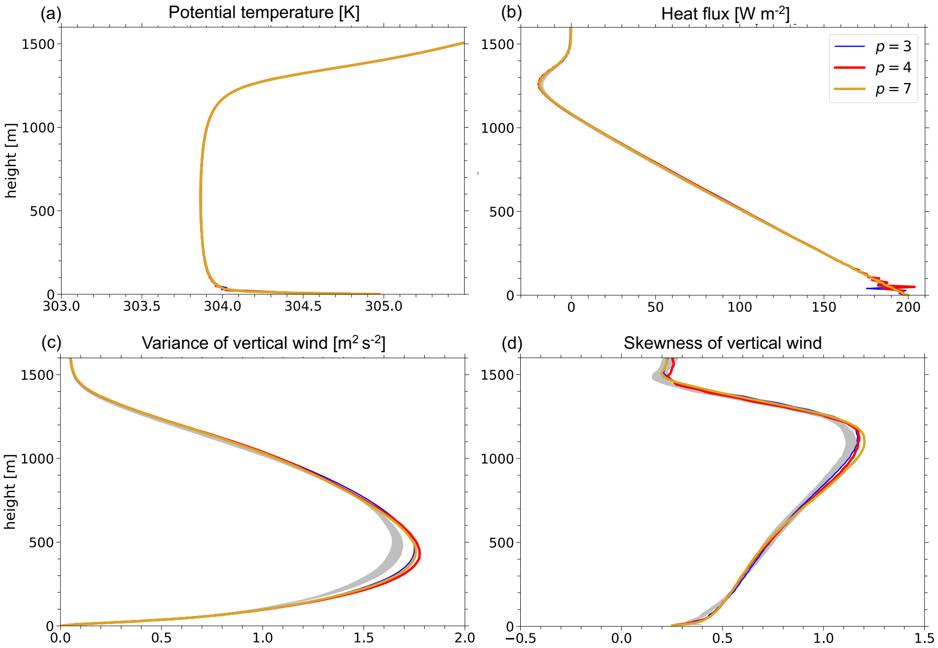

Figure 13. The vertical structure of PBL temporally averaging during the last 30 minutes: (a) potential temperature, (b) resolved eddy heat flux plus SGS heat flux, (c) variable of vertical wind, (d) skewness of vertical wind for $p = 3,4,7$. The gray shade represents the results obtained from KT2023 using the plane model.

4 Conclusions

For conducting future high-resolution atmospheric simulations precisely, our previous studies indicated that conventional low-order discretization methods used in the state-of-the-art global nonhydrostatic dynamical cores have a problem of numerical errors because it is possible to contaminate the effect of physical parameterization schemes. To overcome this issue, we developed a global nonhydrostatic atmospheric dynamical core of dry atmosphere using the discontinuous Galerkin method (DGM) as the spatial discretization considering advantages, such as the simple strategy for the high-order discretization and high computational efficiency in recent parallel supercomputers, over grid-point methods. Furthermore, considering global LES, we formulated a Smagorinsky–Lilly type turbulent model in the cubed sphere coordinate and discretized it in the DGM framework. To validate the proposed global dynamical core, several numerical experiments, from linear advection test to Held–Suarez test, were conducted. To show the high-order numerical convergence, the experimental setup of existing test cases were slightly modified. In addition, an idealized test case was proposed to validate the global dynamical core including the turbulent model. Thorough the numerical experiments with various polynomial orders (p) and spatial resolutions, we discussed the impact of high-order spatial discretization on atmospheric flows.

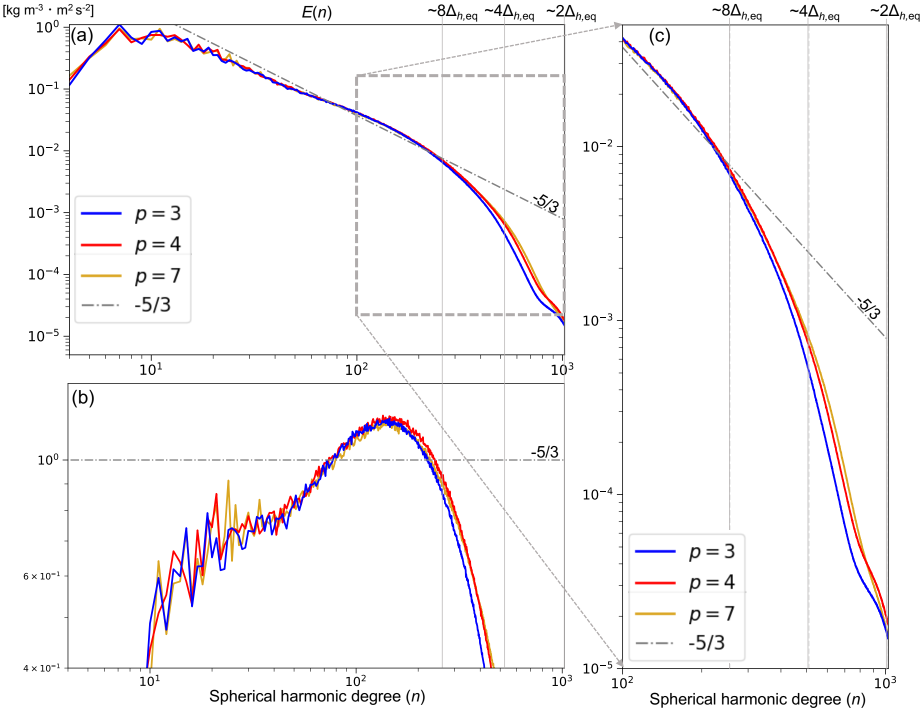

Figure 14. (a) Density-weighted energy spectra $E(n)$ of three-dimensional wind at the height of 500 m for $p = 3,4,7$. The dash-dotted gray line represents $aE(n)$ where $a = 8.0 \times 10^1$. (b) Compensated spectra $E(n)/(an^{-\frac{5}{3}})$. (c) Partial expanded view of energy spectra in the short wavelength range.

575 For the deterministic test cases, such as linear advection and gravity wave test cases, $p+1$-order spatial accuracy was confirmed until the temporal discretization and round-off errors became significant compared to the spatial errors. In the gravity wave test, it was observed that the temporal errors with the third-order HEVI scheme can contaminate the convergence rate of high-order spatial discretization even when using the Courant number against horizontal propagating sound wave of O(0.1). To investigate the numerical performance of terrain-following coordinate with DGM, we conducted a mountain wave test case based on that used in Klemp et al. (2015). However, we made some modifications to investigate high-order numerical convergence. When comparing the results for a fixed DOF, the advantage of large polynomial order is apparent in terms of the fast numerical convergence, although the convergence rate is slightly smaller than the optimal order associated with the spatial discretization. The results of the baroclinic instability test showed that, when $p \geq 3$ and $\Delta_{h,\mathrm{eq}} < 240$ km, the obtained L_2 error norms of surface pressure entered the uncertainty range indicated by the previous studies. We confirmed the rapid numerical convergence over the second-order accuracy until the mature stage was reached. Subsequently, the sharp gradient with the front structure developed and the waves began to break, which made it difficult to identify the numerical convergence with the high-order schemes.

For test cases in which small-scale turbulent structures developed, such as Held–Suarez test and LES experiment of PBL turbulence, we mainly focused on the energy spectra in the terms of effective resolutions. In the Held–Suarez test, where the turbulence model was not used, the extent of dissipation effect with the numerical flux and modal filters is clearly visible; Based on the comparison with the energy spectra for the reference experiment, we confirmed that the effective resolution is improved as the polynomial order increases. When we used high-order modal filters with large decay coefficients to ensure numerical stability during long temporal integration, the effective resolution was estimated to be between about 10~20 grids for $p = 3$ and eight grids for $p = 7, 11$. To enhance the effective resolutions by weakening the modal filters, we consider that entropy stable DGM adopted in Souza et al. (2023) is a promising method, although this topic is beyond the current study. To check the behavior of turbulent model included in global dynamical cores, we proposed an idealized test case of global LES considering a small planet, which is an extension of experimental setup used in KT2021 and KT2023 with the regional plane model. In our numerical experiments with the shallow atmosphere approximation, the convective cell pattern and vertical structures of PBL well reproduce the results of the regional plane model. We confirmed that the obtained energy spectra obey the Kolmogorov spectra of turbulence at the wavelength range longer than about eight grids when $p > 3$ is used together with the Rusanov numerical flux and a sufficiently high-order modal filter; This result is consistent with the numerical criteria discussed in KT2023.

This study indicates the applicability of high-order DGM to global atmospheric dynamical cores via a series of numerical experiments, while several tasks required to conduct actual atmospheric simulations are not performed. To treat the effect of topography in LES, we also need to consider the vertical coordinate transformation in the SGS terms of turbulent model. Such formulation can be achieved using the chain rule, as performed in the differential terms with inviscid fluxes. A related issue is the treatment of topography with steep slopes in high-order strategies. To investigate whether DGM-based dynamical core is robust for realistic topography, a Held-Suarez experiment with realistic topography may be appropriate. Such work is expected to yield deep understandings about the impact of effective resolutions of topography on large-scale flows when high-order DGM is used. Furthermore, it is indispensable to perform a coupling between the physics (such as moist and radiation processes) and DGM-based dynamics. Recent studies begin to discuss the potential difficulties with the element-based methods; For example, in the context of spectral element method, Herrington et al. (2019) indicated that a straightforward evaluation for physics tendencies at irregular nodes within the element causes a grid imprinting along the element boundaries. To solve this problem, they introduced a physics grid with a quasi-equal volume coarser than the node intervals with the dynamics when calculating the physics tendencies. While taking care of the advantages associated with the effective resolutions of high-order dynamical cores, we will explore how to treat the coupling of physics and dynamics in the DGM framework.

Code and data availability. Source codes of SCALE-DG v0.8.0 and setting files for numerical experiments are available at the Zenodo repository (https://doi.org/10.5281/zenodo.10901697), where we have provided scripts to crate figures in this paper. They are provided as open source under the MIT license. SCALE library v.5.5.1 which is a key dependent software of SCALE-DG is available at the Zenodo

Table 1. Values of parameters.

Symbol	Description	Value
C_p	Specific heat for constant pressure of dry air	1.0046×10^4 J K^{-1} kg^{-1}
C_v	Specific heat for constant volume of dry air	7.1760×10^3 J K^{-1} kg^{-1}
R	Gas constant	$C_p - C_v$
P_0	Reference value of pressure	1000 hPa
a	Planetary radius of planet	6.3712×10^3 km
X_r	Factor of reduced planetary radius	166.7
ω	Angular velocity of planet	7.2920×10^{-5} s^{-1}
g	Standard gravitational acceleration	9.8066 m/s^2

Table 2. Double Butcher table for a third-order IMEX RK scheme by Kennedy and Carpenter (2003).

c_s	$a_{ss'}$			
0	0	0	0	0
$\frac{1767732205903}{2027836641118}$	$\frac{1767732205903}{2027836641118}$	0	0	0
$\frac{3}{5}$	$\frac{5535828885825}{10492691773637}$	$\frac{788022342437}{10882634858940}$	0	0
1	$\frac{6485989280629}{16251701735622}$	$-\frac{4246266847089}{9704473918619}$	$-\frac{10755448449292}{10357097424841}$	0
b_s	$\frac{1471266399579}{7840856788654}$	$-\frac{4482444167858}{7529755066697}$	$\frac{11266239266428}{11593286722821}$	$\frac{1767732205903}{4055673282236}$
$\tilde{c}_s$	$\tilde{a}_{ss'}$			
0	0	0	0	0
$\frac{1767732205903}{2027836641118}$	$\frac{1767732205903}{4055673282236}$	$\frac{1767732205903}{4055673282236}$	0	0
$\frac{3}{5}$	$\frac{2746238789719}{10658868560708}$	$-\frac{640167445237}{6845629431997}$	$\frac{1767732205903}{4055673282236}$	0
1	$\frac{1471266399579}{7840856788654}$	$-\frac{4482444167858}{7529755066697}$	$\frac{1767732205903}{11593286722821}$	$\frac{1767732205903}{4055673282236}$
$\tilde{b}_s$	$\frac{1471266399579}{7840856788654}$	$-\frac{4482444167858}{7529755066697}$	$\frac{11266239266428}{11593286722821}$	$\frac{1767732205903}{4055673282236}$

repository (https://doi.org/10.5281/zenodo.10952494), and is subject to the BSD-2-Clause license. Due to large data size, the obtained results from the numerical experiments are saved in the local storage at RIKEN R-CCS.

https://doi.org/10.5194/egusphere-2024-1477
Preprint. Discussion started: 12 June 2024

Table 3. Butcher table for a fourth-order fully explicit RK scheme with ten stages by Ketcheson (2008)

c_s	$a_{ss'}$									
0										
$\frac{1}{6}$	$\frac{1}{6}$									
$\frac{1}{3}$	$\frac{1}{6}$	$\frac{1}{6}$								
$\frac{1}{2}$	$\frac{1}{6}$	$\frac{1}{6}$	$\frac{1}{6}$							
$\frac{2}{3}$	$\frac{1}{6}$	$\frac{1}{6}$	$\frac{1}{6}$	$\frac{1}{6}$						
$\frac{1}{3}$	$\frac{1}{15}$	$\frac{1}{15}$	$\frac{1}{15}$	$\frac{1}{15}$	$\frac{1}{15}$					
$\frac{1}{2}$	$\frac{1}{15}$	$\frac{1}{15}$	$\frac{1}{15}$	$\frac{1}{15}$	$\frac{1}{15}$	$\frac{1}{6}$				
$\frac{2}{3}$	$\frac{1}{15}$	$\frac{1}{15}$	$\frac{1}{15}$	$\frac{1}{15}$	$\frac{1}{15}$	$\frac{1}{6}$	$\frac{1}{6}$			
$\frac{5}{6}$	$\frac{1}{15}$	$\frac{1}{15}$	$\frac{1}{15}$	$\frac{1}{15}$	$\frac{1}{15}$	$\frac{1}{6}$	$\frac{1}{6}$	$\frac{1}{6}$		
1	$\frac{1}{15}$	$\frac{1}{15}$	$\frac{1}{15}$	$\frac{1}{15}$	$\frac{1}{15}$	$\frac{1}{6}$	$\frac{1}{6}$	$\frac{1}{6}$	$\frac{1}{6}$	
b_s	$\frac{1}{10}$	$\frac{1}{10}$	$\frac{1}{10}$	$\frac{1}{10}$	$\frac{1}{10}$	$\frac{1}{10}$	$\frac{1}{10}$	$\frac{1}{10}$	$\frac{1}{10}$	$\frac{1}{10}$

Table 4. Summary of numerical experiments for validating the proposed dynamical core.

Test case	Focus
Linear advection	Validation of the cubed-sphere projection, Convergence rate with advection
Internal gravity wave	Validation of the pressure gradient and buoyancy terms, Convergence rate with wave propagation
Mountain wave	Validation of the terrain-following coordinate, Convergence rate with vertical coordinate transformation
Baroclinic instability	Numerical robustness in developing small-scale flow structures, Numerical convergence discussed in previous studies
Held–Suarez test	Numerical robustness in climatic simulations with long-term integrations, Numerical convergence and effective resolutions
Global LES in a small planet	Validation of the turbulent model formulated in cubed-sphere coordinate, Effective resolutions on energy spectra, Consistency of numerical criterion indicated in KT2023

Appendix A: Additional information for mountain wave test

In this section, we detail the spin-up strategy and sponge layer, which were used in the mountain wave test described in Sect. 3.3. In addition, we consider some reasons why the obtained convergence rate is slightly less than the optimal order accuracy.

Table 5. Modal filter orders and decay coefficients used in the mountain wave test.

	$p_{m,h}$, $p_{m,v}$	$\alpha_{m,h}$, $\alpha_{m,v}$
$p = 3$	32	1.0×10^{-2}
$p = 7$ ($\Delta_{h,\mathrm{eq}} = 625$ m)	64	1×10^{-2}
$p = 7$ ($\Delta_{h,\mathrm{eq}} = 313, 156, 78$ m)	64	5×10^{-3}
$p = 11$ ($\Delta_{h,\mathrm{eq}} = 625$ m)	64	1×10^{-2}
$p = 11$ ($\Delta_{h,\mathrm{eq}} = 313$ m)	64	7.5×10^{-2}
$p = 11$ ($\Delta_{h,\mathrm{eq}} = 156$ m)	64	5×10^{-3}

Table 6. Modal filter orders and decay coefficients used in the baroclinic instability test. Because the vertical resolution was fixed when increasing the horizontal resolution, the decay coefficient for the vertical filter $\alpha_{m,v}$ was reduced in proportion to the timestep.

	$p_{m,h}$	$\alpha_{m,h}$	$p_{m,v}$	$\alpha_{m,v}$ (for $\Delta_{h,\mathrm{eq}} = 250$ km)
$p = 3$	16	2.0×10^{-1}	12	8.0×10^{-1}
$p = 7$	16	2.0×10^{0}	16	1.2×10^{0}
$p = 11$	24	1.6×10^{1}	24	1.6×10^{1}

A1 Spin-up strategy

To mitigate the influence of impulsive start on numerical solutions, we gradually accelerated the wind as performed in previous studies with regional experimental setup. The initial condition is a rest isothermal atmosphere and is represented as

$$\begin{aligned} &u^{\xi} = 0,\ u^{\zeta} = 0,\ u^{\eta} = 0, \\ &p = P_0 \exp\left(-\frac{gz}{RT_0}\right), \\ &\rho = \frac{P_0}{RT_0} \exp\left(-\frac{gz}{RT_0}\right), \end{aligned} \tag{A1}$$

Table 7. Modal filter orders and decay coefficients used in the Held–Suarez test after 250-days spin-up experiments.

	$p_{m,h}$	$\alpha_{m,h}$	$p_{m,v}$	$\alpha_{m,v}$
$p = 3$	8	1.0×10^{-1}	8	5.0×10^{-2}
$p = 7$ ($\Delta_{h,\mathrm{eq}} = 208, 104$ km)	16	4.0×10^{0}	16	4×10^{0}
$p = 7$ ($\Delta_{h,\mathrm{eq}} = 52, 26$ km)	16	5.0×10^{0}	16	5.0×10^{0}
$p = 11$	16	4.0×10^{0}	16	4.0×10^{0}

https://doi.org/10.5194/egusphere-2024-1477
Preprint. Discussion started: 12 June 2024

where $P_0 = 10^5$ Pa and $T_0 = 300$ K. To accelerate a zonal wind, we added the relaxation terms in the right-hand side of governing equations as

$$\begin{aligned}
\frac{\partial \sqrt{G}\rho'}{\partial t} &= \cdots - \alpha_f \sqrt{G}\rho', \\
\frac{\partial \sqrt{G}\rho u^\xi}{\partial t} &= \cdots - \alpha_f \sqrt{G}\left(\rho u^\xi - \rho U^\xi\right), \\
\frac{\partial \sqrt{G}\rho u^\eta}{\partial t} &= \cdots - \alpha_f \sqrt{G}\left(\rho u^\eta - \rho U^\eta\right), \\
\frac{\partial \sqrt{G}\rho u^\zeta}{\partial t} &= \cdots - \alpha_f \sqrt{G}\left(\rho u^\zeta - \rho U^\zeta\right), \\
\frac{\partial \sqrt{G}(\rho\theta)'}{\partial t} &= \cdots - \alpha_f \sqrt{G}(\rho\theta)',
\end{aligned} \tag{A2}$$

where (U^ξ, U^η, U^ζ) are the vector components of prescribed wind and α_f is a time-dependent coefficient with Rayleigh forcing terms. Note that we set the hydrostatic balance part of pressure and density as

$$p_{\mathrm{hyd}} = P_0 \exp\left(-\frac{u_{\mathrm{eq}}}{2RT_0}\sin^2\theta - \frac{gz}{RT_0}\right), \quad \rho_{\mathrm{hyd}} = \frac{p_{\mathrm{hyd}}}{RT_0},$$

which satisfies a dynamically balanced state associated with a zonal wind in solid rotation, $u_{\mathrm{eq}}\cos\theta$. Then, the perturbation at the initial time is given by $p' = p - p_{\mathrm{hyd}}$, $\rho' = \rho - \rho_{\mathrm{hyd}}$.

As the horizontal component of prescribed wind, we consider a zonal wind in solid body rotation where $u_{\mathrm{eq}} = 20$ m s^{-1}. The corresponding (U^ξ, U^η) can be calculated by considering the coordinate conversion between the cubed-sphere and geographic coordinates. To improve the inconsistency with no-flux boundary condition at the surface, we add the vertical component in the form of

$$U^\zeta = -\sqrt{G_v}\left(G_v^{13}U^\xi + G_v^{23}U^\eta\right)\exp\left(-\frac{\zeta}{H_f}\right),$$

where H_f was set to 2 km in this study. This modification also reduces the influence of initial shock. On the other hand, the coefficient with the forcing terms is given as $\alpha_f(t) = w(t)\tau_f^{-1}$, where

$$\begin{aligned}
w &= 1 && \text{for} \quad 0 \le t \le t_1, \\
w &= \frac{1}{2}\left[1 - \cos\left(\pi\frac{t - t_1}{t_2 - t_1}\right)\right] && \text{for} \quad t_1 \le t \le t_2, \\
w &= 0 && \text{for} \quad t \ge t_2,
\end{aligned}$$

and τ_f is the forcing time scale. In this study, these parameters were set as $\tau_f = 60$ s, $t_1 = 200$ s, and $t_2 = 1800$ s.

A2 Sponge layer

To suppress a reflection of waves at the model top, we introduced a sponge layer at upper computational domain. In addition, to reduce the disruption of our targeting structure of mountain wave due to the global propagation of initial shocks, a lateral sponge layer was placed on the 1/4 sector of the sphere. As in Eq. (A2), linear damping terms were added to the governing equations as follows:

$$\frac{\partial \sqrt{G}\rho'}{\partial t} = \cdots - \alpha_s \sqrt{G}\rho',$$

$$\frac{\partial \sqrt{G}\rho u^{\xi}}{\partial t} = \cdots - \alpha_s \sqrt{G}\left(\rho u^{\xi} - U^{\xi}\right),$$

$$\frac{\partial \sqrt{G}\rho u^{\eta}}{\partial t} = \cdots - \alpha_s \sqrt{G}\left(\rho u^{\eta} - \rho U^{\eta}\right),$$

$$\frac{\partial \sqrt{G}\rho u^{\zeta}}{\partial t} = \cdots - \alpha_s \sqrt{G}\left(\rho u^{\zeta} - \rho U^{\zeta}\right),$$

$$\frac{\partial \sqrt{G}(\rho\theta)'}{\partial t} = \cdots - \alpha_s \sqrt{G}(\rho\theta)'.$$

The decay coefficient is given as $\alpha_s = (1 - w(t))(\alpha_{s,h} + \alpha_{s,v})$ where $\alpha_{s,h}$ and $\alpha_{s,v}$ are the coefficients for lateral and upper sponge layers, respectively. To avoid the sponge layer interfering with the initial forcing in Eq. (A2), as the initial forcing weakens, the sponge layer is gradually activated using the coefficient $(1 - w(t))$. The coefficient for the upper sponge layer is given as

$$\alpha_{s,v} = \frac{\tau_{s,v}^{-1}}{2}\left\{\frac{1}{2}\left[1 + \tanh\left(\frac{z - (z_T + z_{\mathrm{sp}})/2}{\delta_{\mathrm{sp},v}(z_T - z_{\mathrm{sp}})}\right)\right]\right\},$$

whereas, for the lateral sponge layer,

$$\alpha_{s,h} = \frac{\tau_{s,h}^{-1}}{2}\left\{\left[1 - \tanh\left(\frac{\lambda - \pi/4}{\delta_{\mathrm{sp},h}\pi/2}\right)\right] + \left[1 + \tanh\left(\frac{\lambda - 7\pi/4}{\delta_{\mathrm{sp},h}\pi/2}\right)\right]\right\}$$
$$\cdot \frac{1}{2}\left[1 + \tanh\left(\frac{|\theta| - \pi/3}{8\pi/180}\right)\right],$$

where z_T is the height of model top, and $\tau^{s,v}$ and $\tau^{s,h}$ are the decay time scales corresponding to the upper and lateral sponge layers. Note that the coefficient for the lateral sponge layer is multiplied by a tapering function in the latitudinal direction to avoid an infinite zonal scale near the poles, as performed in Eq. (20). In this study, we set $z_{\mathrm{sp}} = 15$ km, $\delta_{\mathrm{sp},v} = \delta_{\mathrm{sp},h} = 0.16$, and $\tau_{s,v} = \tau_{s,h} = 100$ s.

A3 Investigation of degrading the optimal numerical convergence

Figure 5 indicates that the convergence rate obtained from the mountain test case is slightly smaller than $p+1$-order accuracy. We consider the reasons behind this result to be as follows; First, to evaluate the differentials with the Jacobian cofactors ($\sqrt{G_v}G_v^{13}$ and $\sqrt{G_v}G_v^{23}$), we used same discretization operator, as described in Sect. 2.3. This strategy is beneficial to simply satisfy the geometric conservation law identity in the discretized equations. However, because the calculated geometric factors have the order p, it is possible to degrade the optimal convergence. Figures A1 (a), (b) show the spatial distribution of numerical errors for vertical wind and the local convergence rate, respectively, for $p = 3$. The numerical error is large near the surface where the mountain exists. Furthermore, the relatively slow convergence rate appears. The rate near the surface is between

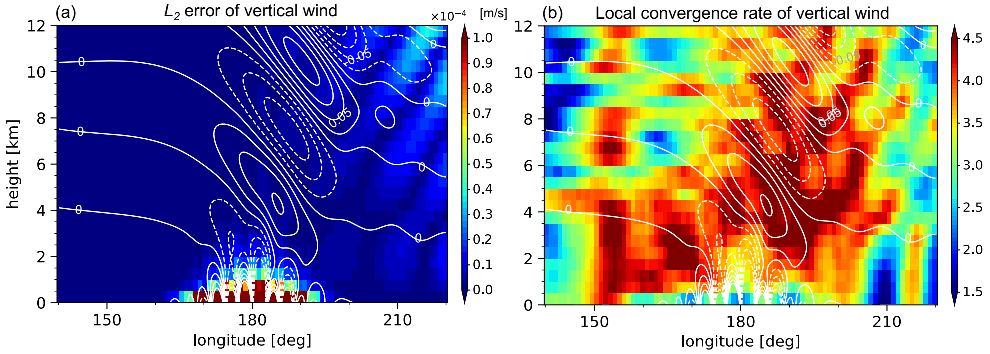

Figure A1. After 2 hours in a mountain wave test case with global model, spatial distribution of (a) L_2 error norm and (b) local convergence rate for the vertical wind at the equator. For the L_2 error norm, we show the result obtained from the experiment where the effective horizontal and vertical grid spacing ($\Delta_{\mathrm{eff},h}, \Delta_{\mathrm{eff},v}$) are set to 156 m and 125 m, respectively, using $p = 3$. The cell color in the figure corresponds to the average values within the finite element. When evaluating the local convergence rate, we used the element average of L_2 error norm obtained from two experiments: a coarse resolution experiment ($\Delta_{\mathrm{eff},h} = 625$ m, $\Delta_{\mathrm{eff},v} = 500$ m) and the highest resolution experiment for $p = 3$ ($\Delta_{\mathrm{eff},h} = 156$ m, $\Delta_{\mathrm{eff},v} = 125$ m). To see the large-scale structure of local convergence rate, moving average was taken across the five elements horizontally. In each figure, the white lines represent the vertical wind in the highest resolution experiment for $p = 3$.

two and three, while it approaches the value of four at locations apart from the surface. Second, the modal filter can reduce the convergence rate during the long-term temporal integrations even if we adopted a high-order modal filter with a relatively small decay coefficient.

To increase the certainty of our speculations, we conducted additional numerical experiments. To simplify the investigations and save the computational resources, we treated the corresponding two-dimensional experimental setup. With respect to the Jacobian cofactors, we considered two cases: (i) the case where it is numerically given by using the same discretization operator mentioned in Sect. 2.3, and (ii) the case when it is given by analytically evaluating the spatial derivatives at the node. In addition, to discuss the impact of modal filters on the convergence rate, we consider the case of no modal filter for $p = 3$ because we found that the 2-hours temporal integration without filters can be somehow performed only for $p = 3$. As performed with the global model case, we conduct a series of numerical experiments changing the spatial resolutions and polynomial orders. To evaluate the error norms, we used the results from the reference experiments with $p = 7$, where $\Delta_{\mathrm{eff},h} = 78$ m and $\Delta_{\mathrm{eff},v} = 62.5$ m ($z < 15$ km).

Figures A2(a), (b) show the spatial distribution of numerical errors for vertical wind and the local convergence rate obtained from the two-dimensional experiments with $p = 3$. As shown in the global experiment (see Fig. A1), the convergence rate near the mountain achieves only the third-order accuracy in the cases of numerically calculated Jacobian cofactor. On the other hand, when the analytical Jacobian cofactor is used, the numerical errors near the mountain decrease and the convergence rate reaches to about fourth-order accuracy. Thus, we confirm that the calculation strategy of Jacobian cofactor is one of reasons for sub-optimal convergence.

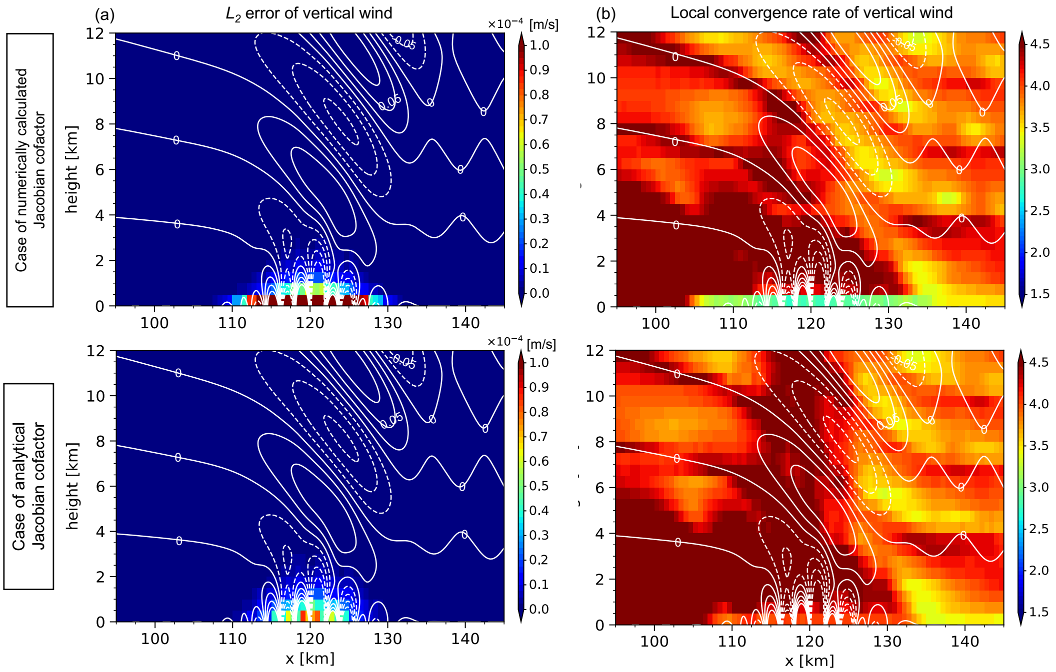

Figure A2. After 2 hours in a **two-dimensional** mountain wave test case, spatial distribution of (a) L_2 error norm and (b) local convergence rate for the vertical wind in the cases of numerically calculated Jacobian cofactor (upper panels) and analytical Jacobian cofactor (lower panels) for $p = 3$. In the L_2 error norm, we show the results obtained from the experiments with $\Delta_{\mathrm{eff},h} = 156$ m and $\Delta_{\mathrm{eff},v} = 125$ m. When evaluating the local convergence rare, we used the results obtained from two experiments: a coarse resolution experiment ($\Delta_{\mathrm{eff},h} = 312$ m, $\Delta_{\mathrm{eff},v} = 250$ m) and the highest resolution experiment for $p = 3$ ($\Delta_{\mathrm{eff},h} = 39$ m, $\Delta_{\mathrm{eff},v} = 31.25$ m). In each figure, the white lines represent the vertical wind in the reference experiment.

Figure A3 shows that the dependence of L_1, L_2, and L_{inf} errors on the spatial resolution. First, we focus on the results with $p = 3$. When the metric cofactors are analytically evaluated and the modal filter is not used, the fourth-order accuracy is observed except for the density. In case of numerically calculated Jacobian cofactor, the convergence rate of L_2 and L_{inf} errors are characterized by the sub-optimal order because the Jacobian cofactors have only pth-order accuracy, as mentioned above. Such behavior is observed for horizontal wind, vertical wind, and the perturbation of potential temperature weighted density based on the comparison between (i) and (ii) cases. On the other hand, the blue and cyan lines indicate that the order reduction with the modal filters is obvious for the horizontal wind, while for other variables, there is little influence. This may be because the filters act on not only the perturbation part of horizontal wind but also on the mean flow part. For higher order cases ($p = 7, 11$), the filters are unavoidable for ensuring numerical stability in classical DGM. Then, the convergence rate can be limited by the modal filters, and the analytical Jacobian cofactor would have little impact. Even for the case (ii), L_2 and L_{inf} errors of horizontal and vertical wind have the convergence rate slightly less than the optimal order. As for the density, note that the third-order accuracy is obtained for $p = 3$ even when using the analytical Jacobian cofactor and removing the modal

https://doi.org/10.5194/egusphere-2024-1477
Preprint. Discussion started: 12 June 2024

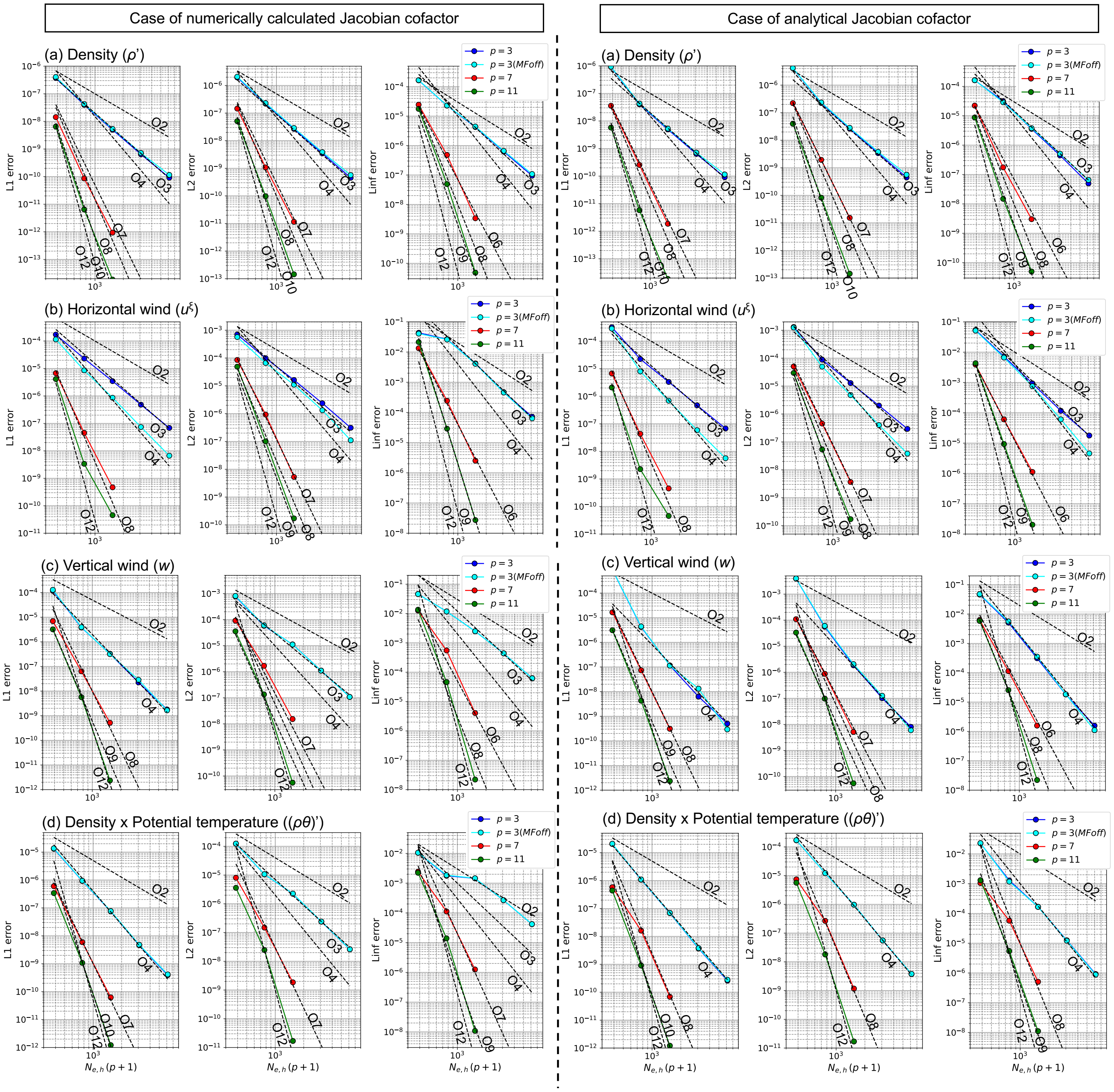

Figure A3. Dependence of L_1, L_2, and $L_{\rm inf}$ errors on spatial resolution for (a) density perturbation (ρ'), (b) horizontal wind (u^{ξ}), (c) vertical wind (w), and (d) perturbation of potential temperature weighted density ($(\rho\theta)'$) after 2 hours in a mountain wave test case with the **two-dimensional experimental setup**. Note that the cyan lines represent the results for the case $p = 3$ without the modal filter (MFoff).

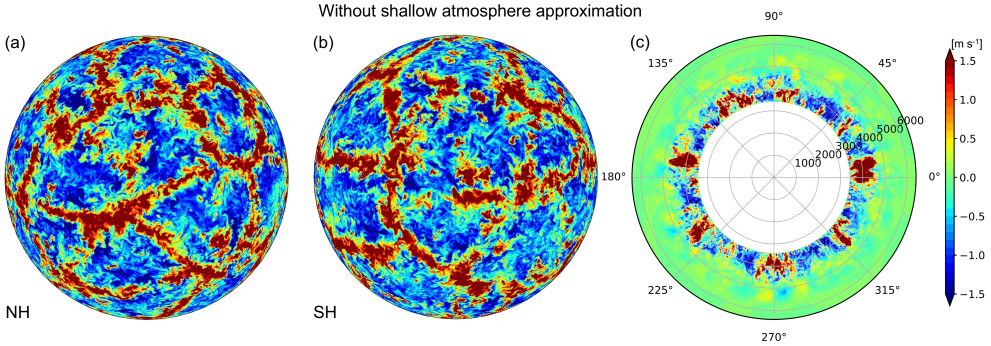

Figure B1. Same as Fig. 12, but these results were obtained without shallow atmosphere approximation. The horizontal distribution for vertical wind at $z = 500$ m after $t = 4$ hours: (a) Northern hemisphere (NH), (b) Southern hemisphere (SH), and (c) the corresponding cross-sections along the equator.

filter. It remains unclear why the density error does not decrease in the optimal order. We may need to pursue how to discretely deal with the hydrostatic balance (e.g., Li and Xing, 2018) and investigate the boundary errors with no-normal flux condition near the surface.

Appendix B: The effect of not using shallow atmosphere approximation on global PBL turbulence experiment

In Sect. 3.6, we showed the results of PBL turbulence experiment with shallow atmosphere approximation. By applying this approximation, the obtained results become comparable with those reported in KT2021 and KT2023 which used the plane regional model. However, because the planetary radius is set to be 3.4 km, this approximation is not suitable for discussing physical aspects such as the impact of sphere geometry on the convective cells. This section shows the results when the shallow atmosphere approximation is not applied.

Figures B1 and B2 show the horizontal distributions of convective cells and vertical structure of PBL when the shallow atmosphere approximation is not applied. In Fig. B2, all results with the shallow atmosphere approximation are represented by the gray shade. An open cell pattern with the characteristic horizontal scale of a few kilometers is observed irrespective of whether we apply the shallow atmosphere approximation. On the other hand, the winds become weaker and the PBL is shallower compared to that in the shallow atmosphere approximation. We consider that such changes are consistent with the effect of spherical geometry because horizontal area increases with the altitude.

Figure B3 shows the energy spectra when the shallow atmosphere approximation is not applied. The major features of energy spectra in the inertia subrange (such as the wavelength range obeyed -5/3 power law and the relation of effective resolution with polynomial order), remain mostly unchanged.

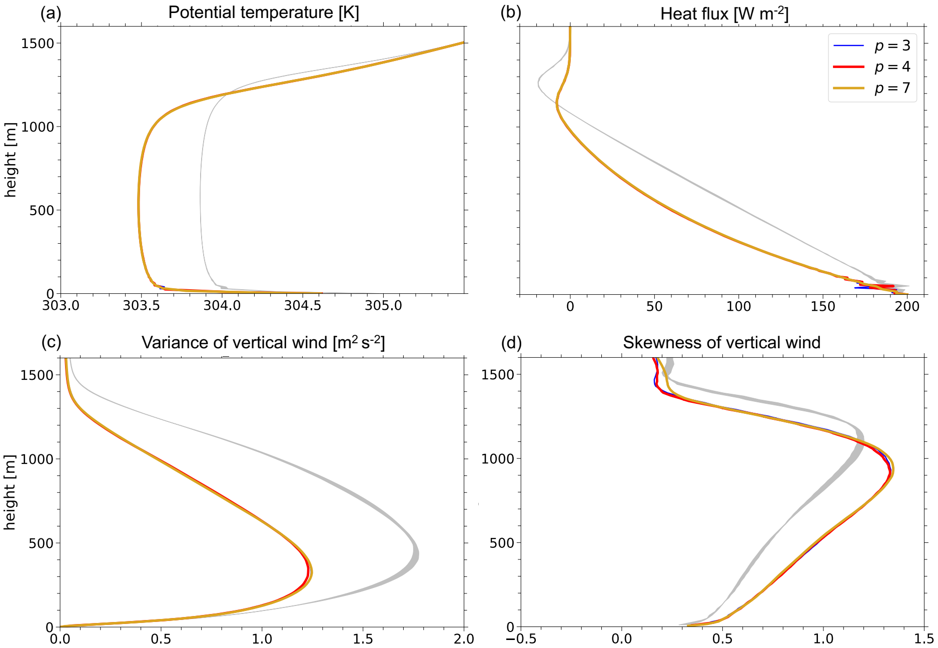

Figure B2. Same as Fig. 13, but figures show the vertical structure of PBL temporally averaged during the last 30 minutes without shallow atmosphere approximation: (a) potential temperature, (b) resolved eddy heat flux plus SGS heat flux, (c) variance of vertical wind, (d) skewness of vertical wind. In these panels, the blue, red, and yellow lines represent the results for $p = 3, 4$, and 7, respectively. We indicate the corresponding results with the shallow atmosphere approximation, shown in Fig. 13, by the gray shade.

Author contributions. All authors have contributed to writing this paper. YK mainly performed the general development of the simulation programs based on DGM and conducted the validation experiments. HT guided this project considering future high-resolution atmospheric simulations and high performance computers. He also contributed to improve the structure of this paper and discuss the simulation results.

Competing interests. The authors have no competing interests to declare.

Acknowledgements. This research was supported by the MEXT KAKENHI (grant number: JP20H05731), Moonshot R&D (grant number: JPMJMS2286), the Foundation for Computational Science (FOCUS) Establishing Supercomputing Center of Excellence, JST AIP (grant number: JPMJCR19U2), JICA and JST SATREPS (grant Number: JPMJSA2109), and JSPS Core-to-Core Program (grant number: JPJSCCA20220001). The experiments in this study were performed using the supercomputer Fugaku at RIKEN (Project ID: ra000005, hp200271, and hp230278) and the Wisteria supercomputer at the University of Tokyo. We thank Dr. Seiya Nishizawa, Dr. Hiroaki Miura, and Dr. Keiichi Ishioka for their valuable comments and suggestions. We would like to thank Editage (www.editage.jp) for English language editing.

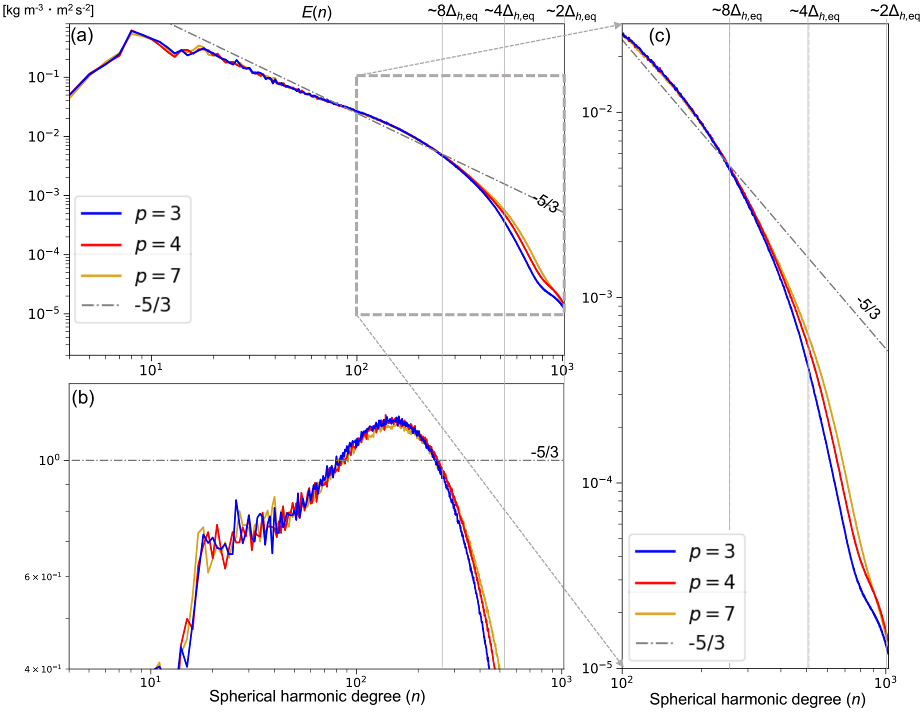

Figure B3. Same as Fig. 14, but figures show the results without shallow atmosphere approximation: (a) Density-weighted energy spectra $E(n)$ of three-dimensional wind at a height of 500 m for $p = 3, 4$, and 7. The dash-dotted gray line represents $aE(n)$ where $a = 8.0 \times 10^1$. (b) Compensated spectra $E(n)/(an^{-\frac{5}{3}})$. (c) Partial expanded view of energy spectra in the short wavelength range.

References

Ascher, U. M., Ruuth, S. J., and Spiteri, R. J.: Implicit-explicit Runge-Kutta methods for time-dependent partial differential equations, Applied Numerical Mathematics, 25, 151–167, https://doi.org/10.1016/S0168-9274(97)00056-1, special Issue on Time Integration, 1997.

Baldauf, M. and Brdar, S.: An analytic solution for linear gravity waves in a channel as a test for numerical models using the non-hydrostatic, compressible Euler equations, Quarterly Journal of the Royal Meteorological Society, 139, 1977–1989, https://doi.org/10.1002/qj.2105, 2013.

Bao, L., Klöfkorn, R., and Nair, R. D.: Horizontally Explicit and Vertically Implicit (HEVI) Time Discretization Scheme for a Discontinuous Galerkin Nonhydrostatic Model, Monthly Weather Review, 143, 972 – 990, https://doi.org/10.1175/MWR-D-14-00083.1, 2015.

Blaise, S., Lambrechts, J., and Deleersnijder, E.: A stabilization for three-dimensional discontinuous Galerkin discretizations applied to nonhydrostatic atmospheric simulations, International Journal for Numerical Methods in Fluids, 81, 558–585, https://doi.org/10.1002/fld.4197, 2016.

Brown, A. R., Derbyshire, S. H., and Mason, P. J.: Large-eddy simulation of stable atmospheric boundary layers with a revised stochastic subgrid model, Quarterly Journal of the Royal Meteorological Society, 120, 1485–1512, https://doi.org/10.1002/qj.49712052004, 1994.

Favre, A.: Turbulence: Space-time statistical properties and behavior in supersonic flows, The Physics of Fluids, 26, 2851–2863, https://doi.org/10.1063/1.864049, 1983.

Gal-Chen, T. and Somerville, R. C.: On the use of a coordinate transformation for the solution of the Navier-Stokes equations, Journal of Computational Physics, 17, 209–228, https://doi.org/10.1016/0021-9991(75)90037-6, 1975.

Gardner, D. J., Guerra, J. E., Hamon, F. P., Reynolds, D. R., Ullrich, P. A., and Woodward, C. S.: Implicit–explicit (IMEX) Runge–Kutta methods for non-hydrostatic atmospheric models, Geoscientific Model Development, 11, 1497–1515, https://doi.org/10.5194/gmd-11-1497-2018, 2018.

Gassner, G. J., Winters, A. R., and Kopriva, D. A.: Split form nodal discontinuous Galerkin schemes with summation-by-parts property for the compressible Euler equations, Journal of Computational Physics, 327, 39–66, https://doi.org/10.1016/j.jcp.2016.09.013, 2016.

Giraldo, F. and Restelli, M.: A study of spectral element and discontinuous Galerkin methods for the Navier–Stokes equations in nonhydrostatic mesoscale atmospheric modeling: Equation sets and test cases, Journal of Computational Physics, 227, 3849–3877, https://doi.org/10.1016/j.jcp.2007.12.009, 2008.

Gottlieb, S., Shu, C.-W., and Tadmor, E.: Strong Stability-Preserving High-Order Time Discretization Methods, SIAM Review, 43, 89–112, https://doi.org/10.1137/S003614450036757X, 2001.

Guerra, J. E. and Ullrich, P. A.: A high-order staggered finite-element vertical discretization for non-hydrostatic atmospheric models, Geoscientific Model Development, 9, 2007–2029, https://doi.org/10.5194/gmd-9-2007-2016, 2016.

Held, I. M. and Suarez, M. J.: A Proposal for the Intercomparison of the Dynamical Cores of Atmospheric General Circulation Models, Bulletin of the American Meteorological Society, 75, 1825 – 1830, https://doi.org/10.1175/1520-0477(1994)075<1825:APFTIO>2.0.CO;2, 1994.

Herrington, A. R., Lauritzen, P. H., Taylor, M. A., Goldhaber, S., Eaton, B. E., Bacmeister, J. T., Reed, K. A., and Ullrich, P. A.: Physics–Dynamics Coupling with Element-Based High-Order Galerkin Methods: Quasi-Equal-Area Physics Grid, Monthly Weather Review, 147, 69 – 84, https://doi.org/10.1175/MWR-D-18-0136.1, 2019.

Hesthaven, J. S. and Warburton, T.: Nodal discontinuous Galerkin methods: algorithms, analysis, and applications, Springer Science & Business Media, https://doi.org/10.1007/978-0-387-72067-8, 2007.

Ishioka, K., Yamamoto, N., and Fujita, M.: A Formulation of a Three-Dimensional Spectral Model for the Primitive Equations, Journal of the Meteorological Society of Japan. Ser. II, 100, 445–469, https://doi.org/10.2151/jmsj.2022-022, 2022.

Jablonowski, C. and Williamson, D. L.: A baroclinic instability test case for atmospheric model dynamical cores, Quarterly Journal of the Royal Meteorological Society, 132, 2943–2975, https://doi.org/10.1256/qj.06.12, 2006.

Kawai, Y. and Tomita, H.: Numerical Accuracy of Advection Scheme Necessary for Large-Eddy Simulation of Planetary Boundary Layer Turbulence, Monthly Weather Review, 149, 2993 – 3012, https://doi.org/10.1175/MWR-D-20-0362.1, 2021.

Kawai, Y. and Tomita, H.: Numerical Accuracy Necessary for Large-Eddy Simulation of Planetary Boundary Layer Turbulence Using the Discontinuous Galerkin Method, Monthly Weather Review, 151, 1479 – 1508, https://doi.org/10.1175/MWR-D-22-0245.1, 2023.

Kennedy, C. A. and Carpenter, M. H.: Additive Runge–Kutta schemes for convection–diffusion–reaction equations, Applied numerical mathematics, 44, 139–181, https://doi.org/10.1016/S0168-9274(02)00138-1, 2003.

Ketcheson, D. I.: Highly Efficient Strong Stability-Preserving Runge–Kutta Methods with Low-Storage Implementations, SIAM Journal on Scientific Computing, 30, 2113–2136, https://doi.org/10.1137/07070485X, 2008.

Klemp, J. B., Skamarock, W. C., and Park, S.-H.: Idealized global nonhydrostatic atmospheric test cases on a reduced-radius sphere, Journal of Advances in Modeling Earth Systems, 7, 1155–1177, https://doi.org/10.1002/2015MS000435, 2015.

Li, G. and Xing, Y.: Well-balanced discontinuous Galerkin methods with hydrostatic reconstruction for the Euler equations with gravitation, Journal of Computational Physics, 352, 445–462, https://doi.org/10.1016/j.jcp.2017.09.063, 2018.

Li, X., Chen, C., Shen, X., and Xiao, F.: Development of a unified high-order nonhydrostatic multi-moment constrained finite volume dynamical core: derivation of flux-form governing equations in the general curvilinear coordinate system, arXiv preprint arXiv:2004.05779, https://doi.org/10.48550/arXiv.2004.05779, 2020.

Lilly, D. K.: On the numerical simulation of buoyant convection, Tellus, 14, 148–172, https://doi.org/10.1111/j.2153-3490.1962.tb00128.x, 1962.

Lin, S.-J. and Rood, R. B.: Multidimensional Flux-Form Semi-Lagrangian Transport Schemes, Monthly Weather Review, 124, 2046 – 2070, https://doi.org/10.1175/1520-0493(1996)124<2046:MFFSLT>2.0.CO;2, 1996.

Lin, S.-J. and Rood, R. B.: An explicit flux-form semi-Lagrangian shallow-water model on the sphere, Quarterly Journal of the Royal Meteorological Society, 123, 2477–2498, https://doi.org/10.1002/qj.49712354416, 1997.

Malardel, S. and Wedi, N. P.: How does subgrid-scale parametrization influence nonlinear spectral energy fluxes in global NWP models?, Journal of Geophysical Research: Atmospheres, 121, 5395–5410, https://doi.org/10.1002/2015JD023970, 2016.

Miyamoto, Y., Kajikawa, Y., Yoshida, R., Yamaura, T., Yashiro, H., and Tomita, H.: Deep moist atmospheric convection in a subkilometer global simulation, Geophysical Research Letters, 40, 4922–4926, https://doi.org/10.1002/grl.50944, 2013.

Nair, R. D.: Diffusion Experiments with a Global Discontinuous Galerkin Shallow-Water Model, Monthly Weather Review, 137, 3339 – 3350, https://doi.org/10.1175/2009MWR2843.1, 2009.

Nair, R. D., Thomas, S. J., and Loft, R. D.: A Discontinuous Galerkin Transport Scheme on the Cubed Sphere, Monthly Weather Review, 133, 814 – 828, https://doi.org/10.1175/MWR2890.1, 2005.

Nishizawa, S., Yashiro, H., Sato, Y., Miyamoto, Y., and Tomita, H.: Influence of grid aspect ratio on planetary boundary layer turbulence in large-eddy simulations, Geoscientific Model Development, 8, 3393–3419, https://doi.org/10.5194/gmd-8-3393-2015, 2015.

Orgis, T., Läuter, M., Handorf, D., and Dethloff, K.: Baroclinic waves on the β plane using low-order Discontinuous Galerkin discretisation, Journal of Computational Physics, 339, 461–481, https://doi.org/10.1016/j.jcp.2017.03.029, 2017.

Phillips, N. A.: A COORDINATE SYSTEM HAVING SOME SPECIAL ADVANTAGES FOR NUMERICAL FORECASTING, Journal of Atmospheric Sciences, 14, 184 – 185, https://doi.org/10.1175/1520-0469(1957)014<0184:ACSHSS>2.0.CO;2, 1957.

Rančić, M., Purser, R. J., and Mesinger, F.: A global shallow-water model using an expanded spherical cube: Gnomonic versus conformal coordinates, Quarterly Journal of the Royal Meteorological Society, 122, 959–982, https://doi.org/10.1002/qj.49712253209, 1996.

Rančić, M., Purser, R. J., Jović, D., Vasic, R., and Black, T.: A Nonhydrostatic Multiscale Model on the Uniform Jacobian Cubed Sphere, Monthly Weather Review, 145, 1083 – 1105, https://doi.org/10.1175/MWR-D-16-0178.1, 2017.

Ronchi, C., Iacono, R., and Paolucci, P.: The “Cubed Sphere”: A New Method for the Solution of Partial Differential Equations in Spherical Geometry, Journal of Computational Physics, 124, 93–114, https://doi.org/10.1006/jcph.1996.0047, 1996.

Rusanov, V. V.: Calculation of Interaction of Non-Steady Shock Waves with Obstacles, Journal of Computational and Mathematical Physics USSR, 1, 267, https://doi.org/10.1016/0041-5553(62)90062-9, 1961.

Sadourny, R.: Conservative Finite-Difference Approximations of the Primitive Equations on Quasi-Uniform Spherical Grids, Monthly Weather Review, 100, 136 – 144, https://doi.org/10.1175/1520-0493(1972)100<0136:CFAOTP>2.3.CO;2, 1972.

Satoh, M., Tomita, H., Yashiro, H., Miura, H., Kodama, C., Seiki, T., Noda, A. T., Yamada, Y., Goto, D., Sawada, M., et al.: The Non-hydrostatic Icosahedral Atmospheric Model: Description and development, Progress in Earth and Planetary Science, 1, 18, https://doi.org/10.1186/s40645-014-0018-1, 2014.

Satoh, M., Stevens, B., Judt, F., Khairoutdinov, M., Lin, S.-J., Putman, W. M., and Düben, P.: Global Cloud-Resolving Models, Current Climate Change Reports, 5, 172–184, https://doi.org/10.1007/s40641-019-00131-0, 2019.

Schär, C., Leuenberger, D., Fuhrer, O., Lüthi, D., and Girard, C.: A New Terrain-Following Vertical Coordinate Formulation for Atmospheric Prediction Models, Monthly Weather Review, 130, 2459 – 2480, https://doi.org/10.1175/1520-0493(2002)130<2459:ANTFVC>2.0.CO;2, 2002.

Skamarock, W. C., Klemp, J. B., Duda, M. G., Fowler, L. D., Park, S.-H., and Ringler, T. D.: A Multiscale Nonhydrostatic Atmospheric Model Using Centroidal Voronoi Tesselations and C-Grid Staggering, Monthly Weather Review, 140, 3090–3105, https://doi.org/10.1175/MWR-D-11-00215.1, 2012.

Smagorinsky, J.: GENERAL CIRCULATION EXPERIMENTS WITH THE PRIMITIVE EQUATIONS: I. THE BASIC EXPERIMENT, Monthly Weather Review, 91, 99–164, https://doi.org/10.1175/1520-0493(1963)091<0099:GCEWTP>2.3.CO;2, 1963.

Souza, A. N., He, J., Bischoff, T., Waruszewski, M., Novak, L., Barra, V., Gibson, T., Sridhar, A., Kandala, S., Byrne, S., Wilcox, L. C., Kozdon, J., Giraldo, F. X., Knoth, O., Marshall, J., Ferrari, R., and Schneider, T.: The Flux–Differencing Discontinuous Galerkin Method Applied to an Idealized Fully Compressible Nonhydrostatic Dry Atmosphere, Journal of Advances in Modeling Earth Systems, 15, e2022MS003 527, https://doi.org/10.1029/2022MS003527, 2023.

Sridhar, A., Tissaoui, Y., Marras, S., Shen, Z., Kawczynski, C., Byrne, S., Pamnany, K., Waruszewski, M., Gibson, T. H., Kozdon, J. E., Churavy, V., Wilcox, L. C., Giraldo, F. X., and Schneider, T.: Large-eddy simulations with ClimateMachine v0.2.0: a new open-source code for atmospheric simulations on GPUs and CPUs, Geoscientific Model Development, 15, 6259–6284, https://doi.org/10.5194/gmd-15-6259-2022, 2022.

Tolstykh, M., Shashkin, V., Fadeev, R., and Goyman, G.: Vorticity-divergence semi-Lagrangian global atmospheric model SL-AV20: dynamical core, Geoscientific Model Development, 10, 1961–1983, https://doi.org/10.5194/gmd-10-1961-2017, 2017.

Tomita, H. and Satoh, M.: A new dynamical framework of nonhydrostatic global model using the icosahedral grid, Fluid Dynamics Research, 34, 357–400, https://doi.org/10.1016/j.fluiddyn.2004.03.003, 2004.

Ullrich, P. and Jablonowski, C.: Operator-Split Runge–Kutta–Rosenbrock Methods for Nonhydrostatic Atmospheric Models, Monthly Weather Review, 140, 1257 – 1284, https://doi.org/10.1175/MWR-D-10-05073.1, 2012a.

Ullrich, P. A.: A global finite-element shallow-water model supporting continuous and discontinuous elements, Geoscientific Model Development, 7, 3017–3035, https://doi.org/10.5194/gmd-7-3017-2014, 2014.

Ullrich, P. A. and Jablonowski, C.: MCore: A non-hydrostatic atmospheric dynamical core utilizing high-order finite-volume methods, Journal of Computational Physics, 231, 5078 – 5108, https://doi.org/10.1016/j.jcp.2012.04.024, 2012b.

Ullrich, P. A., Jablonowski, C., Kent, J., Lauritzen, P. H., Nair, R. D., and Taylor, M. A.: Dynamical core model intercomparison project (DCMIP) test case document, DCMIP Summer School, 83, https://api.semanticscholar.org/CorpusID:197412504, 2012.

Wan, H., Giorgetta, M. A., and Bonaventura, L.: Ensemble Held–Suarez Test with a Spectral Transform Model: Variability, Sensitivity, and Convergence, Monthly Weather Review, 136, 1075 – 1092, https://doi.org/10.1175/2007MWR2044.1, 2008.

Wan, H., Giorgetta, M. A., Zängl, G., Restelli, M., Majewski, D., Bonaventura, L., Fröhlich, K., Reinert, D., Rípodas, P., Kornblueh, L., and Förstner, J.: The ICON-1.2 hydrostatic atmospheric dynamical core on triangular grids – Part 1: Formulation and performance of the baseline version, Geoscientific Model Development, 6, 735–763, https://doi.org/10.5194/gmd-6-735-2013, 2013.

Williamson, D. L., Drake, J. B., Hack, J. J., Jakob, R., and Swarztrauber, P. N.: A standard test set for numerical approximations to the shallow water equations in spherical geometry, Journal of Computational Physics, 102, 211–224, https://doi.org/10.1016/S0021-9991(05)80016-6, 1992.

Winters, A. R., Moura, R. C., Mengaldo, G., Gassner, G. J., Walch, S., Peiro, J., and Sherwin, S. J.: A comparative study on polynomial dealiasing and split form discontinuous Galerkin schemes for under-resolved turbulence computations, Journal of Computational Physics, 372, 1–21, https://doi.org/10.1016/j.jcp.2018.06.016, 2018.

Yi, T.-H. and Giraldo, F. X.: Vertical Discretization for a Nonhydrostatic Atmospheric Model Based on High-Order Spectral Elements, Monthly Weather Review, 148, 415 – 436, https://doi.org/10.1175/MWR-D-18-0283.1, 2020.

Zängl, G., Reinert, D., Rípodas, P., and Baldauf, M.: The ICON (ICOsahedral Non-hydrostatic) modelling framework of DWD and MPI-M: Description of the non-hydrostatic dynamical core, Quarterly Journal of the Royal Meteorological Society, 141, 563–579, https://doi.org/10.1002/qj.2378, 2015.